Journal of Materials Chemistry A

ROYAL SOCIETY OF CHEMISTRY

REVIEW

View Article Online
View Journal | View Issue

Cite this: J. Mater. Chem. A, 2020, 8, 485

Recent progress in g-C_3N_4 quantum dots: synthesis, properties and applications in photocatalytic degradation of organic pollutants

Teng Wang,†[a] Chunyang Nie,†[a] Zhimin Ao,*[a] Shaobin Wang[b] and Taicheng An[a]

Received 15th October 2019
Accepted 28th November 2019

DOI: 10.1039/c9ta11368a

rsc.li/materials-a

Graphitic-carbon nitride quantum dots (g-C_3N_4QDs), as a rising star in the carbon nitride family, show great potential in many fields involving bioimaging, fuel cells, and photo(electro)catalysis, due to their fascinating optical and electronic properties. Especially, the efficient light capture, tunable photoluminescence and extraordinary up-conversion photoluminescence properties of g-C_3N_4QDs may offer promising potential for full utilization of the solar spectrum, thus promoting their applications in photocatalytic reactions. Some reviews on g-C_3N_4 have been presented; while most of them have concentrated on g-C_3N_4 in 3-dimensional (3D) or 2D structures, few focused on g-C_3N_4QDs. Therefore, this review aims to summarize the recent advances in g-C_3N_4QDs regarding their synthesis, optical and electronic properties and photocatalytic applications for degrading organic pollutants. Moreover, crucial issues in g-C_3N_4QD future application in these flourishing research areas are discussed, with prospects towards the final realization of efficient and long-term stable g-C_3N_4QD-based photocatalysts.

1. Introduction

Photocatalysis is considered as a promising solution to the ever growing energy shortage and environmental pollution since solar energy is sustainable and green.[1] Photocatalytic reactions have been demonstrated to be effective for obtaining hydrogen from water splitting,[2] mineralization of organic pollutants,[3–7] disinfection of bacteria,[8–11] reduction of carbon dioxide,[12] *etc.* In photocatalytic processes, the photocatalyst is the key component. Historically, metallic semiconductors with a response to ultraviolet (UV) light including TiO_2, CdS, ZnO, and GaP have been commonly used as photocatalysts in various photocatalytic technologies.[13] However, many metallic resources on the Earth are not renewable, and some metals are harmful to the environment and human health,[14,15] such as Pb, Co, *etc.*

[a]Guangdong Key Laboratory of Environmental Catalysis and Health Risk Control, Guangzhou Key Laboratory of Environmental Catalysis and Pollution Control, School of Environmental Science and Engineering, Institute of Environmental Health and Pollution Control, Guangdong University of Technology, Guangzhou 51006, People's Republic of China. E-mail: zhimin.ao@gdut.edu.cn

[b]University of Adelaide, School of Chemical Engineering, Adelaide, SA 5005, Australia

† These authors contributed equally.

Mr Teng Wang is now pursuing a Master's degree under the supervision of Prof. Zhimin Ao at the School of Environmental Science and Engineering, Institute of Environmental Health and Pollution Control, Guangdong University of Technology. His current research interests include the synthesis of g-C_3N_4 quantum dot composites and their applications in gas phase photocatalysis.

Dr Chunyang Nie obtained her Master's degree in 2013 from East China Normal University (China) and PhD degree in 2016 from Universite Paul Sabatier (France) under the supervision of Dr Emmanuel Flahaut and Dr Marc Monthioux. She joined Prof. Ao's group at the Guangdong University of Technology in 2016 as a Postdoctoral Fellow. Her current research interests focus on the synthesis of novel carbon-based catalysts for aqueous organic pollutant remediation and study of the corresponding catalytic mechanisms.

Therefore, metal-free photocatalysts are of great importance. On the other hand, visible light and near-infrared (NIR) light activated photocatalysts are very attractive because the proportion of visible and NIR light in the solar spectrum is over 97%, much higher than that of UV light (~3%).[16]

Polymeric graphitic carbon nitride ($g\text{-}C_3N_4$) was firstly demonstrated as a suitable heterogeneous catalyst for Friedel–Crafts reactions in 2006 [17] and it became the research focus of photocatalysis in 2009 when it was discovered to be a good metal-free photocatalyst (band gap = 2.7 eV) for water splitting under visible light.[18] Subsequently, $g\text{-}C_3N_4$ was widely applied as a photocatalyst for solar energy transfer, water purification and so on.[19]

The story of $g\text{-}C_3N_4$ could be dated back to 1834 when Berzelius first synthesized a polymeric derivative of C_3N_4 and Liebig named it melon.[20] Melon is considered as a linear polymer consisting of connected tri-*s*-triazines *via* secondary nitrogen rather than interconnected tri-*s*-triazines *via* tertiary amines contained in 2-dimensional (2D) $g\text{-}C_3N_4$ sheets. The structure of $g\text{-}C_3N_4$ is similar to that of graphene, where N heteroatoms substitute C atoms in the graphene framework forming π-conjugated systems containing sp^2 hybridized N and C atoms. However, the stacking distance of two layers in $g\text{-}C_3N_4$ (d = 0.326 nm) is slightly higher than that in crystalline graphite.[21] In addition, the interplanar interaction between layers in $g\text{-}C_3N_4$ is somehow stronger than that in graphite, which accounts for the good chemical stability of $g\text{-}C_3N_4$ in most solvents.[22] Moreover, $g\text{-}C_3N_4$ is only composed of carbon and nitrogen elements that are both abundant on the Earth, which enables its easy and controllable synthesis at low cost. Up to now, $g\text{-}C_3N_4$ has been commonly synthesized by pyrolysis of carbon-rich and nitrogen-rich precursors such as cyanamide,[23] melamine,[24] and urea[25] *via* condensation or bulk reactions. A large number of articles and reviews on the synthesis and applications of $g\text{-}C_3N_4$ could be found elsewhere.[21,26,27]

Despite the aforementioned advantages, bulk $g\text{-}C_3N_4$ still encounters several drawbacks including a low specific surface area and poor quantum yield, which are not beneficial to its practical applications in various photocatalytic reactions.[28] To address these issues, a lot of efforts to engineer the nanostructure of $g\text{-}C_3N_4$ (nanosheets, mesoporous, hollow spheres, and nanorods) or introduce heteroatoms (metals or non-metals) into bulk $g\text{-}C_3N_4$ were made.[21,22,29–31] Furthermore, peculiar optical and electronic properties can be induced when the size of bulk $g\text{-}C_3N_4$ is diminished down to 10 nm to obtain quantum dots (QDs) or nanoribbons because strong quantum confinement and edge effects can occur with such a small size.[32] For instance, the conduction and valence bands of $g\text{-}C_3N_4$QDs are shifted in opposite directions with respect to bulk $g\text{-}C_3N_4$, resulting in a wider band gap and a significant difference in the

Prof. Zhimin Ao received his PhD in Materials Science from Jilin University, China in 2008. He is currently a full professor at the Institute of Environmental Health and Pollution Control, School of Environmental Science and Engineering, Guangdong University of Technology. His research interests mainly focus on the development of environmental catalysts and corresponding mechanism investigation. He has published over 100 SCI papers with citations over 3600 times and an H index of 29. He serves as an Associate Editor of Frontiers in Nanotechnology.

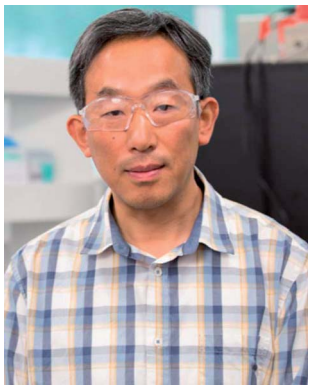

Prof. Shaobin Wang obtained his PhD in Chemical Engineering from the University of Queensland, Australia. He is now a Professor at the School of Chemical Engineering, The University of Adelaide, Australia. His research interests focus on nanomaterial synthesis and application for adsorption and catalysis, fuel and energy conversion and environmental remediation. He has published more than 400 refereed journal papers with citations over 27 000 and an H-index of 93. He is a Global Highly Cited Researcher in Chemical/Environmental Engineering for 2016, 2017 and 2018.

Professor Taicheng An received his PhD in Environmental Science from Sun Yat-sen University, China in 2002. He is currently a full professor and the director of the Institute of Environmental Health and Pollution Control, Guangdong University of Technology. His research interests mainly focus on: (1) synthesis, characterization, optimization and application of nanostructured catalysts and natural mineral materials in environmental remediation; (2) applications of advanced oxidation processes (AOPs); (3) the transportation mechanisms, fate prediction and health effect of emerging organic contaminants. He has had over 70 patents and published over 360 referred research papers. He serves as an Associate Editor of Appl. Catal. B: Environ. and Ctr. Rev. Env. Tech.

photophysical properties and photoexcited charge carriers for g-C_3N_4QDs.[33] Therefore, g-C_3N_4QDs and g-C_3N_4QD-based composites have been commonly applied for photocatalytic water splitting,[28,34] photo(electro)catalytic abatement of organic pollutants,[35–37] and other reactions.[38–40]

On the other hand, semiconductor QDs have been applied for optoelectronic devices, biological labelling, *etc.* in the past few years owing to their excellent fluorescence performance and biochemical properties.[41–47] However, conventional QDs have caused some serious health and environmental concerns due to the use of heavy metals as the essential elements, which limits their wide application. Consequently, considerable attention has been paid to develop new metal-free QDs with similar optical properties. Various studies on the preparation of carbon-based QDs like carbon nanodots, graphene QDs, and g-C_3N_4QDs have been carried out. Compared to carbon nanodots and graphene QDs, g-C_3N_4QDs exhibit a higher photoluminescence (PL) quantum yield,[33,48] which makes them better candidates as biosensors.[49–52] As a result, more and more efforts have been devoted to the synthesis and potential applications of g-C_3N_4QDs in recent years. Hence, it is necessary to provide reviews summarizing the synthesis methods of g-C_3N_4QDs and elaborating their potential applications in diverse fields. In contrast to the plentiful reviews on the synthesis, properties and various applications of bulk g-C_3N_4 and g-C_3N_4 nanosheets, relevant articles on g-C_3N_4QDs have been barely documented in the literature.

Herein, a comprehensive overview on the recent progress in the synthesis and applications of g-C_3N_4QD-based photocatalysts is presented. First, the preparation of g-C_3N_4QDs by different methods is summarized and their advantages and disadvantages are systematically compared. Next, the optical properties of g-C_3N_4QDs including optical absorption and PL are thoroughly discussed. Furthermore, this review is dedicated to the applications of g-C_3N_4QD-based composite photocatalysts in the abatement of organic pollutants. Finally, some concluding remarks and prospects on the future research of g-C_3N_4QD-based photocatalysts are given.

2. Synthesis strategy of g-C_3N_4QDs

The strategy of synthesizing g-C_3N_4QDs is similar to that of carbon-based QDs, which can be classified into two routes depending on the size development of the precursors: top-down and bottom-up routes (as shown in Fig. 1). For the top-down route, the synthesis of g-C_3N_4QDs is started from macroscopic g-C_3N_4 structures, followed by a series of treatments including sonication,[44,47,53–61] hydrothermal treatment,[28,36,38,40,46,62–70] and evaporation–condensation and hydrolysis approaches.[33,45] to form 2D nanosheets, 1D nanowires or nanoribbons, and finally to obtain 0D QDs. For the bottom-up route, g-C_3N_4QDs are obtained using carbon and nitrogen sources as a precursor by solid phase reactions,[39,43,71–79] the microwave-assisted solvothermal method,[41,42,80–89] and quasi-chemical vapor deposition (CVD).[34,90] For example, the nitrogen source is urea or thiourea, and the carbon source is citric acid, sucrose or glucose. Herein, the representative g-C_3N_4QD preparation methods and their advantages and disadvantages are revealed in Table 1.

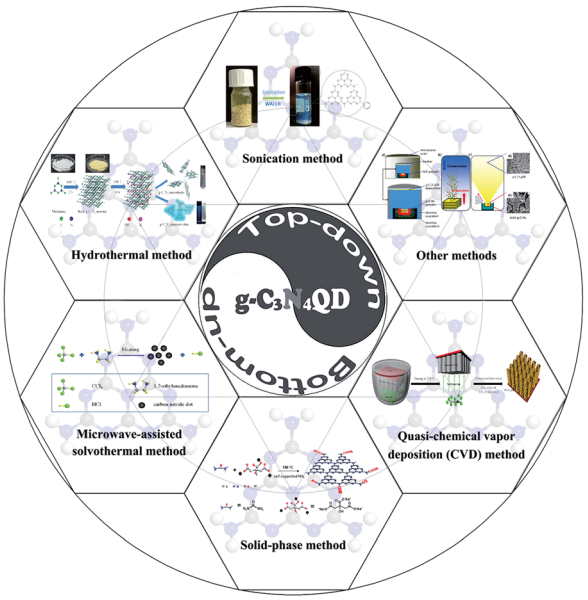

Fig. 1 A schematic of g-C_3N_4QD preparation *via* "top down" and "bottom up" routes.

2.1 Top-down route

2.1.1. Sonication method. It has been reported that ultrasonic waves can generate both low pressure and high pressure waves in a liquid, which gives rise to the formation and collapse of smaller vacuum bubbles.[15] The cavitation leads to a high-speed impact jet, forming a strong hydrodynamic shear force.[44,56,58] Therefore, the energy of the ultrasound can be utilized to exfoliate bulk 3D g-C_3N_4 into 2D nanosheets, 1D nanowires or nanoribbons, and finally into 0D QDs. For instance, sonication of a water suspension of bulk g-C_3N_4, which was prepared by calcination of dicyandiamide for 10 h, was employed by Yuan and co-workers to obtain g-C_3N_4QDs.[56] Notably, the resulting product from sonication was actually a composite of g-C_3N_4QDs and g-C_3N_4 nanosheets in which QDs with diameters below 10 nm were embedded in the nanosheets forming a heterojunction. Li *et al.*[58] reported the synthesis of pure phenyl-modified g-C_3N_4QDs by sonicating an aqueous suspension of bulk g-C_3N_4 containing phenyl groups, followed by a centrifugation step to remove the un-stripped bulk g-C_3N_4. More precisely, the as-prepared products should be described as g-C_3N_4 nanosheets because atomic force microscopy (AFM) and transmission electron microscopy (TEM) observations revealed that the nanosheets have a large diameter (several tens of nanometers) with a thickness of 5–6 nm (Fig. 2a–c). Photographs of phenyl-modified g-C_3N_4QD powder with a yellow color and aqueous solution of QDs are shown in Fig. 2d. The modification with phenyl groups on g-C_3N_4QDs can influence the π-electron delocalization in the conjugated carbon nitride network, resulting in a high quantum yield up to 48.4% in the aqueous suspension and a much higher Stokes shift than that

Table 1 Comparison of the advantages and disadvantages of different g-C_3N_4QD preparation methods

	Methods	Merits	Demerits	Ref.
Top-down	One-step sonication method	Simple steps and easy operation	Low yield and long synthesis cycle	44, 53–56, 58, 60 and 61
	Sonication coupled with chemical oxidation	Good yield and high purity	High cost and complicated steps	47, 57 and 59
	One-step hydrothermal method	Simple steps and low cost	Low yield and long synthesis cycle	35, 36, 38, 40, 46, 62, 65, 67, 68 and 70
	Hydrothermal coupled with chemical oxidation	Good yield and high purity	High cost and complicated steps	28, 63, 66 and 69
Bottom-up	Solid-phase method	High yield, high quantum yield, and adjustable PL performance	Time-consuming in purification post-treatment	39, 43 and 71–79
	Microwave-assisted solvothermal method	Simple steps, short synthesis cycle and low cost	Low quantum yield	41, 42 and 80–89
	Quasi-chemical vapor deposition (CVD) method	Closely integrated when preparing composite materials	High energy consumption and demands further separation and purification post-treatments	34 and 90

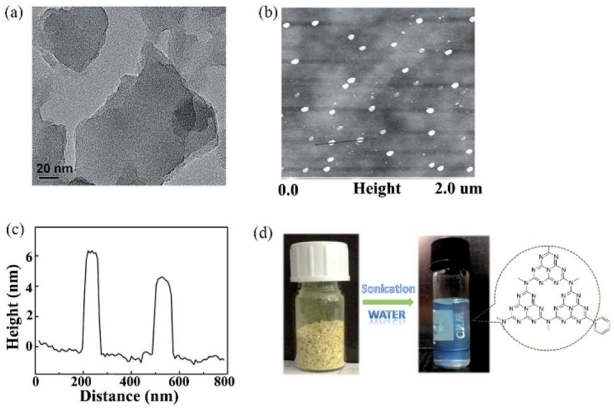

Fig. 2 (a) TEM image and (b) AFM image of the synthetized phenyl modified g-C_3N_4QDs. (c) The corresponding height profile of two random nanoparticles from the AFM image of phenyl modified g-C_3N_4QDs. (d) Illustration of the preparation of a phenyl modified g-C_3N_4QD colloidal aqueous suspension. Reprinted with permission from ref. 58. Copyright 2016 WILEY-VCH Verlag GmbH & Co. KGaA, Weinheim.

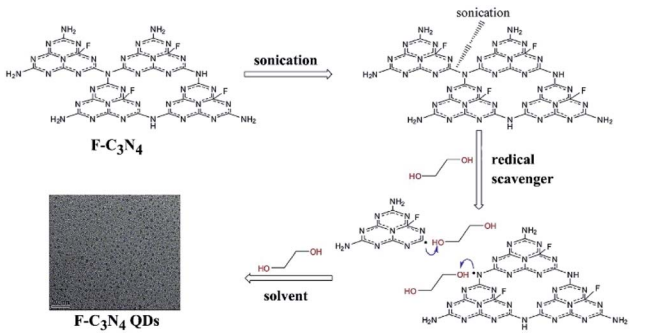

Fig. 3 Schematic illustration of the formation of F-C_3N_4 quantum dots in ethylene glycol. Reprinted with permission from ref. 44. Copyright 2016 Elsevier Ltd.

of reported carbon nitride based fluorophores.[58] Another example of synthesizing g-C_3N_4QDs by sonication was reported by Ai's group.[44] To improve the performance of QDs, they fabricated fluorine-doped g-C_3N_4QDs (F-C_3N_4QDs) from bulk fluorine-doped g-C_3N_4 (F-C_3N_4) prepared with melamine and ammonia fluoride precursors. Notably, F-C_3N_4 was exfoliated in ethylene glycol instead of water during the sonication process (Fig. 3). The ethylene glycol solvent played two roles in the fabrication: (i) preventing the recombination of F-C_3N_4 sheets by scavenging the active C and N radials contained in the F-C_3N_4 sheets; (ii) limiting the aggregation of QDs due to the suitable viscosity of ethylene glycol. The prepared F-C_3N_4QDs have a size distribution of 1.5–2.0 nm in the ethylene glycol solvent and present a higher fluorescence intensity than pure g-C_3N_4QDs.[44]

It should be noted that sonication treatment can also be coupled with other methods to exfoliate bulk g-C_3N_4 into g-C_3N_4QDs. Several studies reported a combination of a chemical oxidation method with sonication for the synthesis of g-C_3N_4QDs.[47,57,59] Generally, bulk g-C_3N_4 is firstly oxidized into porous g-C_3N_4 using acids with a strong oxidizing ability and then exfoliated into porous nanosheets under high temperature and high pressure. Afterwards, an ultrasound bath treatment is performed to break up the nanosheets into QDs, followed by a final purification step with centrifugation and dialysis. Xie *et al.*[47] used a mixture of concentrated H_2SO_4 and HNO_3 to treat bulk g-C_3N_4 and then a hydrothermal treatment on the oxidized products dispersed in concentrated ammonia hydroxide solution to prepare porous g-C_3N_4 nanosheets. Finally, the nanosheets were sonicated in water, forming QDs (Fig. 4a). The as-prepared g-C_3N_4QDs show a diameter distribution ranging from 2–6 nm with the highest proportion at 4 nm and an average thickness of ~0.35 nm, which is close to the thickness of a C–N monolayer (Fig. 4b–d). In addition, the surface of such single-layered QDs is negatively charged,

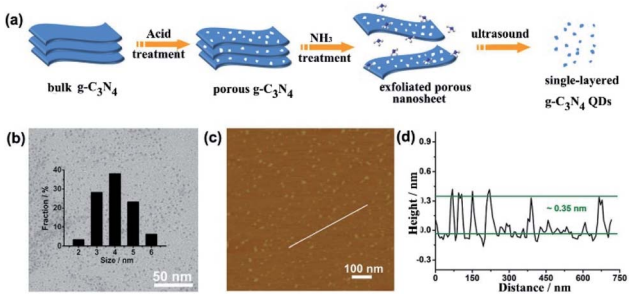

Fig. 4 (a) Schematic illustration of the strategy for the preparation of g-C_3N_4QDs. (b) TEM image and the corresponding size distribution of the g-C_3N_4QDs. (c) and (d) AFM and corresponding height image of the g-C_3N_4QDs. Reprinted with permission from ref. 47. Copyright 2014 WILEY-VCH Verlag GmbH & Co. KGaA, Weinheim.

which makes the g-C_3N_4QD suspension particularly stable in a few weeks. Zhang *et al.*[57] reported the preparation of single-layered g-C_3N_4QDs by a similar modified Hummers' method (Fig. 5a). Briefly, a large amount of bulk g-C_3N_4 and sodium nitrate was firstly oxidized with concentrated H_2SO_4 at room temperature, forming an intermediate with a chain-like structure and was further oxidized with potassium permanganate in order to obtain smaller flakes of g-C_3N_4 nanosheets. Subsequently, the resultant products were dispersed in ice water containing hydrogen peroxide. Finally, QDs were obtained by ultrasonication. With this modified Hummers' method, the QDs show a thickness of ~0.4 nm with a large diameter of 31 nm (Fig. 5b–e).

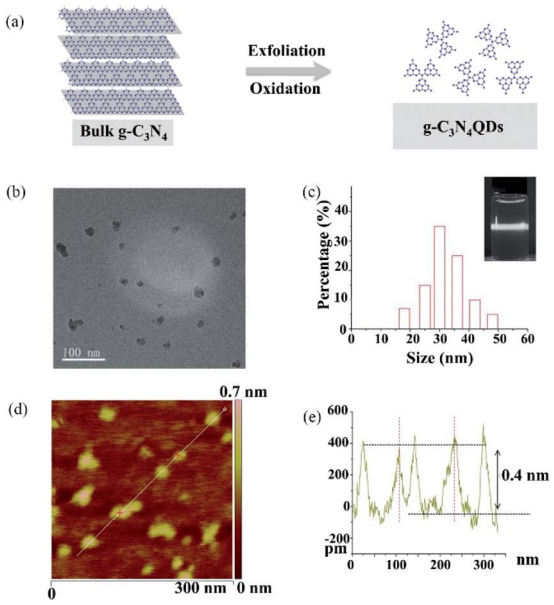

Fig. 5 (a) Proposed synthetic protocol for the g-C_3N_4QDs. (b) The TEM image and (c) size distribution of the g-C_3N_4QDs; the inset of (c) shows the Tyndall effect of the g-C_3N_4QD aqueous dispersion. A representative AFM image (d) and the corresponding height analysis (e) along the lines marked in the AFM image. Reprinted with permission from ref. 57. Copyright 2015 The Royal Society of Chemistry.

2.1.2. Hydrothermal method. The hydrothermal method as a simple, green and economical technique has been widely employed to synthesize various nanomaterials including QDs.[35,36,38,40,46,62,65,67,68,70] By taking advantage of the thermal shear force under high temperature and high pressure, 3D g-C_3N_4 can also be gradually exfoliated into 0D QDs with a hydrothermal fluid. Zhan *et al.*[46] proposed a simple one-step hydrothermal synthesis of g-C_3N_4QDs, in which bulk g-C_3N_4 was initially dispersed in a mixture of concentrated KOH and ethanol solution and the resulting suspension was then transferred into an autoclave and heated at 180 °C for 16 h (Fig. 6a). It should be pointed out that the presence of KOH not only facilitates the exfoliation of g-C_3N_4 resulting from the intercalation of potassium and hydroxyl into layers but also helps the oxidization of the edges of g-C_3N_4 sheets. The as-prepared g-C_3N_4QDs only consist of a monolayer or a few layers of g-C_3N_4 sheets and their average diameter was ~3.3 nm (Fig. 6b–d).

Similar to the sonication method, hydrothermal treatment can also be combined with other pre-treatments like chemical oxidation to fabricate g-C_3N_4QDs.[28,63,66,69] Wang *et al.*[28] used oxidation of bulk g-C_3N_4 in air to destroy the hydrogen bonds between the g-C_3N_4 layers and obtain g-C_3N_4 nanosheets, which were then subjected to acidic etching with concentrated H_2SO_4 and HNO_3 for cleaving the nanosheets into nanoribbons with widths less than 10 nm, and a final hydrothermal reaction was conducted to generate g-C_3N_4QDs (Fig. 7a). The resultant g-C_3N_4QDs have particle sizes ranging from 5 to 9 nm, well-crystallized structures and good water solubility (Fig. 7b–d). Recently, Jin *et al.*[66] took a similar approach to prepare g-C_3N_4QDs and fabricated a composite electrode of ZnO nanowire arrays coated with the as-prepared g-C_3N_4QDs for photocatalytic water splitting. In addition, Li *et al.* described a two-step synthesis of g-C_3N_4QDs involving a prior chemical oxidation and a subsequent hydrothermal treatment.[63] Compared to Wang's work,[28] the QDs fabricated by Li *et al.* are much larger

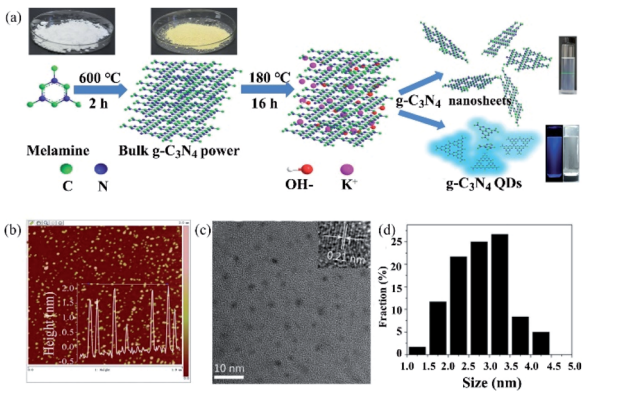

Fig. 6 (a) Schematic illustration of the synthesis of size-controlled g-C_3N_4 nanosheets and QDs *via* ethanol-thermal treatment in the presence of KOH. (b) AFM image of the g-C_3N_4QDs (inset: height profile along the white line corresponding to the AFM image). (c) HRTEM image of g-C_3N_4QDs. (d) Size distribution of g-C_3N_4QDs. Reprinted with permission from ref. 46. Copyright 2017 The Royal Society of Chemistry and the Centre National de la Recherche Scientifique.

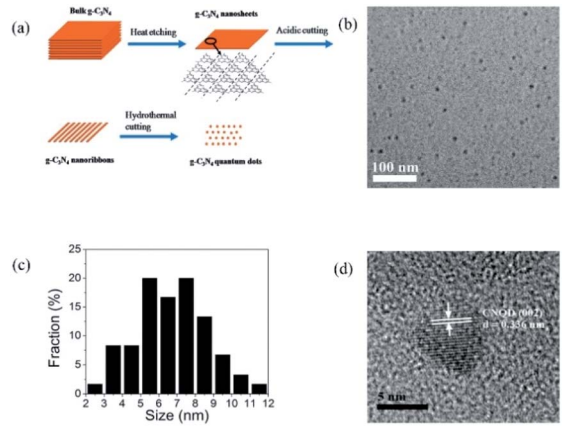

Fig. 7 (a) Schematic illustration of the controllable synthesis of g-C_3N_4 nanosheets, nanoribbons and QDs. (b) TEM images of g-C_3N_4QDs; (c) diameter distribution of the g-C_3N_4QDs; (d) HRTEM image of a single g-C_3N_4QD. Reprinted with permission from ref. 28. Copyright 2014 The Royal Society of Chemistry.

(the mean size is ~20 nm), suggesting that a previous thermal oxidation treatment is favorable to the preparation of smaller g-C_3N_4QDs.

2.1.3. Other methods. Besides the aforementioned methods, one-pot evaporation–condensation and hydrolysis approaches have also been reported.[33,45] Han *et al.*[45] used a household microwave oven to heat a crucible containing a mixture of bulk g-C_3N_4 powder and silicon carbide particles for 5 min, followed by centrifugation to remove the large particles from g-C_3N_4QDs (Fig. 8). During this evaporation–condensation process, silicon carbide particles can provide sufficient vibrational kinetic energy for the cleavage of g-C_3N_4 layers, resulting in the formation of small g-C_3N_4 pieces for the further generation of QDs. Compared with the conventional methods, this microwave-assisted approach is easier and less time-consuming and it can reach a yield of g-C_3N_4QDs as high as 40%. Moreover, the produced g-C_3N_4QDs exhibit high crystallinity, excellent fluorescence, and relatively concentrated size distribution. Because of those advantages, this evaporation–condensation approach may be considered as a potential strategy for the large-scale synthesis of g-C_3N_4QDs. Zhang and co-workers[33] used H_2O, which is a protic solvent to initiate the hydrolysis of bulk g-C_3N_4 in H_2SO_4 solution, to obtain a mixture of g-C_3N_4QDs and g-C_3N_4 nanoleaves. The resultant QDs possess a narrow size distribution varying from 2 to 4 nm and the resultant nanoleaves show a length ranging from 200 to 500 nm. Interestingly, the authors found that g-C_3N_4 nanorods could also be prepared by using another protic solvent, *i.e.*, CH_3OH. More importantly, the as-prepared g-C_3N_4QDs exhibited a superior quantum yield of 46%, much higher than that of most g-C_3N_4QDs prepared by other methods.

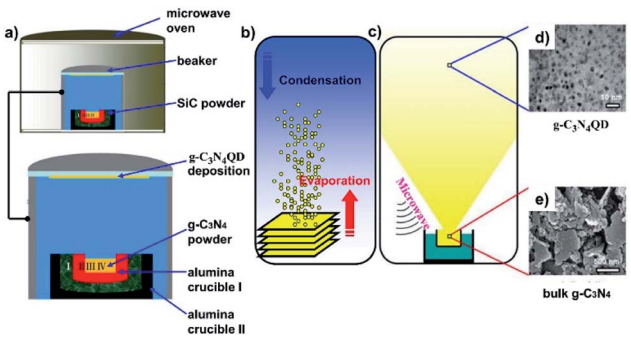

Fig. 8 Schematic illustration of (a) the fabrication device, (b) the evaporation–condensation process, and (c) distribution of g-C_3N_4(g) during the transport process. (d) TEM image of the as-prepared g-C_3N_4QDs. (e) SEM image of bulk g-C_3N_4. Reprinted with permission from ref. 45. Copyright 2017 Elsevier B.V.

2.2 Bottom-up route

2.2.1. Microwave-assisted solvothermal method. The first reported synthesis of g-C_3N_4QDs was realized by the microwave-assisted solvothermal method.[88] The heat energy generated from microwave irradiation can destroy the chemical bonds in the carbon-containing and nitrogen-containing precursors and trigger polymerization or carbonization to rapidly form g-C_3N_4QDs. Meanwhile, uniform thermal energy can be provided by the microwave irradiation, which ensures that the size of the generated QDs is evenly distributed.[91–93] Therefore, the microwave-assisted solvothermal method has been widely employed to prepare g-C_3N_4QDs due to its high efficiency and low cost. In the pioneering work,[88] microwave heating of a mixture of CCl_4 and 1,2-ethylenediamine (EDA) was conducted and photoluminescence g-C_3N_4QDs with diameters of 2–4 nm (Fig. 9) were obtained. Note that reflux heating or solvothermal heating of CCl_4 and EDA can also result in g-C_3N_4QDs. Later on, a large-scale synthesis of fluorescent g-C_3N_4QDs by heating *N*,*N*-dimethylformamide solution[80] or organic amines like dimethylamine, ethylamine or tripropylamine in the presence of acids including chlorosulfonic acid,

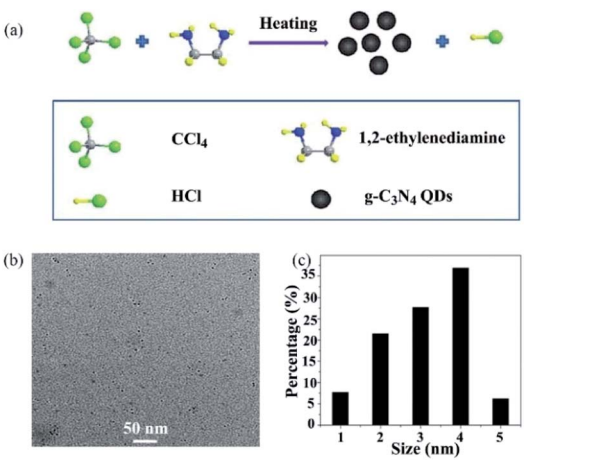

Fig. 9 (a) A schematic (not to scale) illustrating the formation process of g-C_3N_4QDs. (b) TEM image and (c) the corresponding particle size distribution histograms of the g-C_3N_4QDs obtained by refluxing a mixture of CCl_4 and EDA at 80 °C for 60 min. Reprinted with permission from ref. 88. Copyright 2011 The Royal Society of Chemistry.

H_2SO_4, HCl, or HNO_3 under microwave irradiation was reported.[84] In addition, the fabrication of g-C_3N_4QDs with a narrow size distribution by the microwave-assisted solvothermal method with single or two organic precursors including formamide, chitosan, guanidine hydrochloride and EDTA, folic acid, citrate and urea or thiourea was also found in the literature.[41,42,81–86] Especially, with the amine-terminated precursor (chitosan) or sulfur-containing precursor (thiourea), the synthesis of amino-functionalized or sulfur and oxygen co-doped g-C_3N_4QDs is accomplished. These QD samples exhibit good dispersion in water and strong fluorescence and thus show potential applications in the detection of ions or chlorine in water and bioimaging.

On the other hand, hydrothermal treatment can also provide the required energy for the formation of g-C_3N_4QDs starting from organic precursors. He and co-workers employed a one-pot hydrothermal synthesis to carbonize 1-butyl-3-methylimidazolium ([Bmim]BF_4), a typical ionic liquid (IL), in water and obtained QDs with a mean diameter of 4.15 ± 1.95 nm.[87] However, the fractions of C and N elements in the resultant QDs are determined to be 48.97 and 8.56 wt%, respectively, from elemental analysis. Hence, the IL-derived QDs are defined as CNQDs rather than g-C_3N_4QDs.

2.2.2. Solid-phase method. Previous studies have shown that solid-state organic precursors can be decomposed by heat energy and then turned into carbon QDs.[94] In a similar fashion, g-C_3N_4QDs can be prepared by a solid-phase method. Particularly, the elemental composition, surface functional groups, size and defect degree of the synthesized QDs can be modified by changing the ratio of the carbon and nitrogen sources, making the optical properties of g-C_3N_4QDs tunable.[39,43,71–78,95] In addition, the solid-phase method offers the merits of easy operation, cost-effectiveness, a solvent-free approach and high tolerance to the precursors. Zhou *et al.*[73] firstly launched the solid-phase method for the preparation of g-C_3N_4QDs, in which sodium citrate and urea were heated in an autoclave at 180 °C for 1 h. Because the decomposition of urea generates a large quantity of ammonia to increase the vessel pressure, sodium citrate is then decomposed and reacts with the decomposed urea, inducing the formation of g-C_3N_4QDs (Fig. 10a). Well-crystallized QDs with an average size of 4.3 nm and a typical topographic height of 1.5–2.5 nm were generated (Fig. 10b–d). Remarkably, such g-C_3N_4QDs show good water stability, strong blue fluorescence and a high quantum yield of 42%, which are mainly attributed to the presence of defects and the oxygen-containing functional groups in QDs. Moreover, the authors observed that the increased carbon content in g-C_3N_4QDs by decreasing the molar ratio of urea to sodium citrate from 12 : 1 to 9 : 1 resulted in a slight red-shift of the emission peak, while a further decrease of the molar ratio between the two reactants led to an obvious blue-shift of the emission peak due to the increase of oxygen-rich groups on the surface of QDs. Subsequently, utilization of other precursors such as urea and citric acid, thiourea and sodium citrate, and melamine and EDTA to prepare g-C_3N_4QDs with different characteristics by the solid phase method has been also reported.[43,72,75,95] For instance, Li *et al.*[95] obtained sulfur-doped g-C_3N_4QDs (SCNQDs) starting

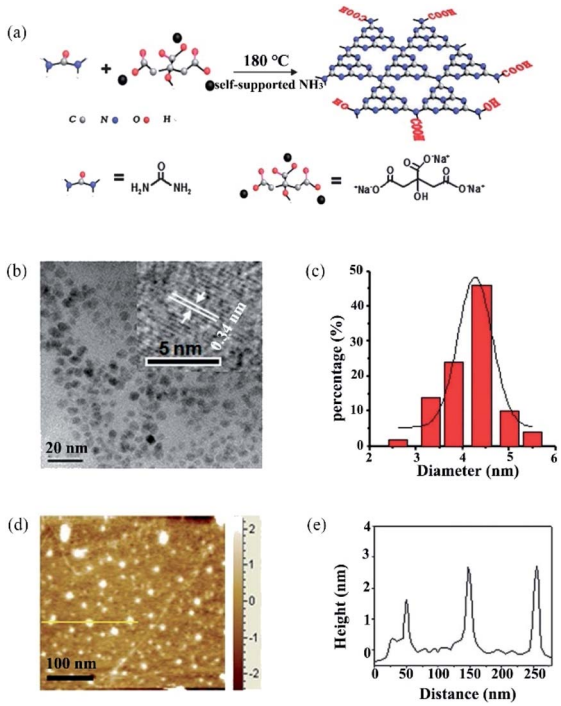

Fig. 10 (a) Mechanism for the formation of highly fluorescent g-C_3N_4QDs. (b) TEM image of the g-C_3N_4QDs. The inset shows a representative HR-TEM image of an individual carbon nitride dot. (c) Size distribution histogram of g-C_3N_4QDs. (d) AFM image of g-C_3N_4QDs deposited on a mica substrate and (e) the height profile along the line in (d). Reprinted with permission from ref. 73. Copyright 2013 The Royal Society of Chemistry.

from thiourea and sodium citrate and the doped QDs show a smaller average diameter and slightly increased light absorption edge compared to the un-doped QDs (Fig. 11).

2.2.3. Quasi-chemical vapor deposition (CVD). In the quasi-CVD method, a substrate is generally placed on the top of a crucible and the carbon and nitrogen-containing precursor is placed at the bottom of the crucible. Upon thermal heating of the crucible in a furnace, the precursor is sublimated and then decomposed into QDs on the substrate. In this way, composites of substrate/g-C_3N_4QDs are synthesized directly. To collect pure g-C_3N_4QDs, the substrate deposited with QDs is usually immersed in a suitable solvent and then sonicated to peel QDs off the substrate. So far, g-C_3N_4QDs with a TiO_2 nanotube array (TiO_2-NTA) substrate *via* a quasi-CVD process have been reported.[34,90] Li *et al.*[34] and An *et al.*[90] obtained composites of TiO_2-NTAs/g-C_3N_4QDs by heating melamine or dicyandiamide at 550 °C for several hours, respectively (Fig. 12). It is well known that the thermal decomposition of melamine or dicyandiamide can result in the formation of g-C_3N_4.[96] Surprisingly, during the quasi-CVD process the small molecules produced from the decomposition of the precursor only polymerize into QDs, and the TiO_2-NTA substrate can prevent the further polymerization of QDs into large particles or nanosheets. It is interesting to note that g-C_3N_4QDs confined in the interior of TiO_2-NTAs were observed in Li's work while g-C_3N_4QDs decorated on the surface of TiO_2-NTAs were demonstrated by An *et al.* Such a discrepancy

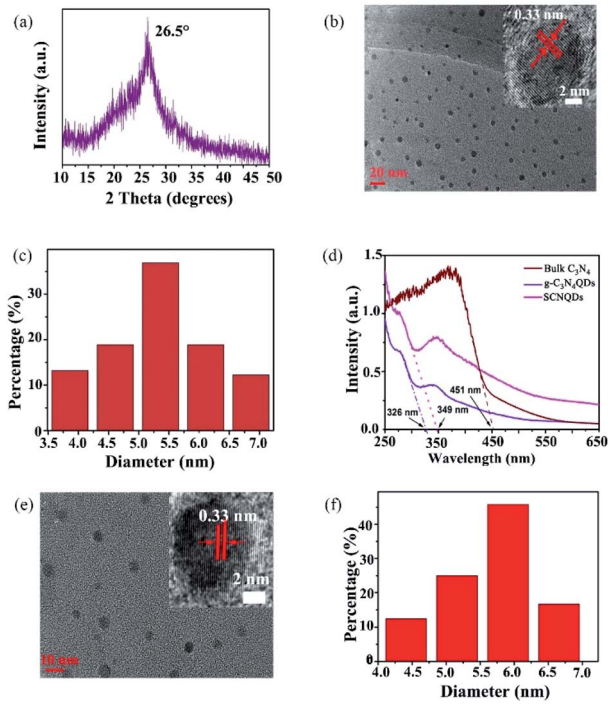

Fig. 11 (a) The XRD pattern of the prepared SCNQDs. (b) TEM images of SCNQDs (the inset in (b) shows a high resolution image of bare SCNQDs) and (e) g-C_3N_4QDs, the size distribution of (c) SCNQDs and (f) g-C_3N_4QDs, and (d) the UV-vis absorption spectra of bulk C_3N_4, g-C_3N_4QD and SCNQD powders. Reprinted with permission from ref. 95. Copyright 2017 World Scientific Publishing Company.

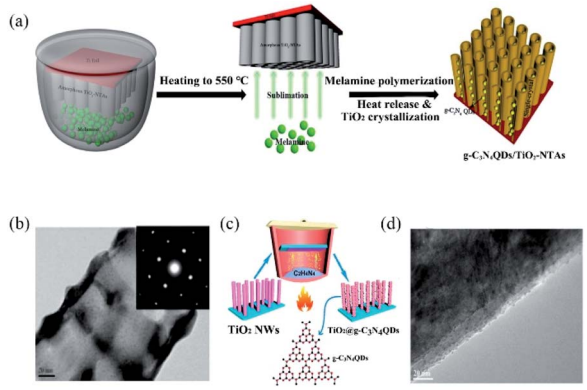

Fig. 12 (a) A schematic illustrating the fabrication of g-C_3N_4QDs/TiO_2-NTAs. (b) TEM and SAED (inset) images of g-C_3N_4QDs in g-C_3N_4QDs/TiO_2-NTAs. Reprinted with permission from ref. 34. Copyright 2015 Elsevier Ltd. (c) Schematic illustration of the CVD process for the synthesis of g-C_3N_4QDs on TiO_2-NTAs in an aluminum crucible device. (d) TEM of TiO_2-NTAs/g-C_3N_4QDs. Reprinted with permission from ref. 90. Copyright 2016 American Chemical Society.

possibly results from the different structures of the two TiO_2-NTA samples prepared by different methods. In addition, the mean diameter of g-C_3N_4QDs encapsulated inside TiO_2-NTAs is estimated to be ~2.4 nm, lower than that of QDs coated on the TiO_2-NTAs (~5 ± 2 nm), implying that the confinement effect in the interior of TiO_2-NTAs is stronger.

2.3 Summary of the synthesis of g-C_3N_4QDs

Overall, both top-down and bottom-up methods are feasible for g-C_3N_4QD synthesis and they show different advantages and disadvantages. In terms of cost, the microwave-assisted solvothermal method and solid phase method are the most economical methods among them due to the low demand on equipment and relatively simple and quick synthesis. However, the stoichiometry and bond configurations of QDs produced from the two bottom-up methods may be different from those of g-C_3N_4. As for the one-step sonication method and one-step hydrothermal method, although they are easy operations and require low-cost equipment, the long synthesis cycle increases the electricity consumption and thus increases the cost. Especially when they are combined with chemical oxidation pretreatments for attaining a higher yield, the cost of g-C_3N_4QD production is further increased. The Quasi-CVD method should be the most expensive method among the abovementioned methods because of the higher demand on equipment, energy consumption and low yield. However, this method can produce composite materials with good contact between g-C_3N_4QDs and the substrate *via* a single step. Moreover, g-C_3N_4QDs prepared by different methods probably show different structural properties and surface chemistry like average diameters, surface functionalities, element compositions and defective structures, which affects the electronic structures and optical properties of the as-prepared g-C_3N_4QDs accordingly and makes these QDs act differently in practical applications. For example, the g-C_3N_4QDs prepared by the hydrothermal method exhibit strong blue light emission and special upconversion photoluminescence behavior. These properties can be used as spectral conversions in photocatalytic systems.[28] In addition, with a microwave-assisted solvothermal method, the synthesis of g-C_3N_4QDs and doped QDs can be realized simultaneously by selecting suitable precursors. The resultant g-C_3N_4QD samples have good dispersibility and strong fluorescence in water and therefore show potential applications in the bioimaging and detection of ions or chlorine in water. Additionally, compared to the bottom-up method, the yield of QDs given by the top-down method is usually lower. Therefore, g-C_3N_4QDs prepared by the top-down method are often combined with other materials to obtain composites used as photo(electro)catalysts, fuel cell electrodes and so on, whereas the g-C_3N_4QDs prepared by the bottom-up method are mostly employed for biosensing, biological imaging, *etc.*

3. Properties

Due to the special electronic structure and quantum size effect, g-C_3N_4QDs show fascinating optical properties, including photoluminescence, chemiluminescence and adjustable light absorption, making them appealing photocatalysts for hydrogen evolution and degradation of pollutants.

3.1 Optical absorption

g-C_3N_4QDs generally exhibit a broad optical absorption ranging from the UV to the visible region with the characteristic

absorption peak centered in the UV region (Fig. 13). Compared to bulk g-C_3N_4, the absorption pattern of g-C_3N_4QDs shows a significant blue shift, which is likely ascribed to the opposite movement of the conduction band and valence band induced by the size effect.[33] For instance, g-C_3N_4QDs produced from a microwave heat-treatment of dimethylamine show a strong absorption band at 262 nm (Fig. 13a).[84] Occasionally, absorption shoulders arising from the introduction of oxygen groups or heteroatoms into g-C_3N_4QDs are present in the absorption spectra.[63,65,73] For example, g-C_3N_4QDs synthesized by the low-temperature solid-phase method[34] show two absorption peaks located around 240 nm and 344 nm, respectively (Fig. 13b). The first peak is assigned to the π–π* electronic transitions of carbon nitrides consisting of *s*-triazine rings and the second peak originates from the conjugated carbonyl groups or carbonyl moieties. Wu *et al.* observed two peaks in the absorption spectrum of phosphorus doped g-C_3N_4QDs centered at 230 nm and 402 nm, respectively, whereas the latter was attributed to the n–π* transition of the p-π orbital between the phosphorus atoms and *s*-triazine rings.[65]

3.2 Photoluminescence (PL)

As a class of emerging metal-free fluorescent nanomaterials, the unique PL of g-C_3N_4QDs has offered enormous opportunities for applications in photocatalysis and other fields. In general,

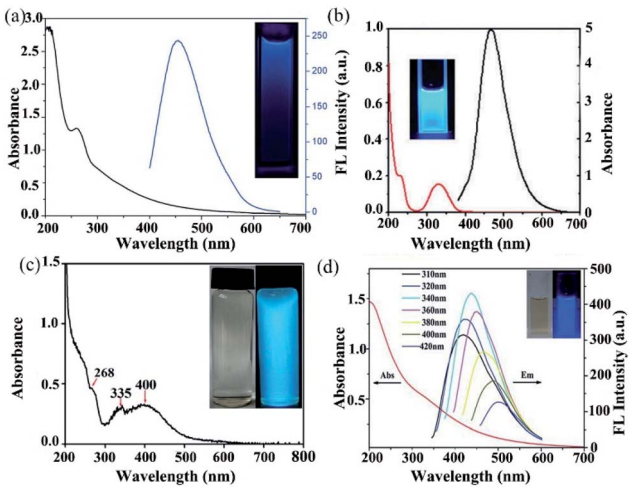

Fig. 13 (a) UV-vis absorption (black) and photoluminescence (blue) spectra of the g-C_3N_4QD dispersion. Inset: photograph of the g-C_3N_4QD dispersion under UV light (365 nm). Reprinted with permission from ref. 84, Copyright 2012 The Royal Society of Chemistry. (b) UV-vis absorption (red line) and photoluminescence (black line) spectra of the obtained g-C_3N_4QDs. The inset shows a digital picture of the g-C_3N_4QD dispersed in pure water. Reprinted with permission from ref. 73, Copyright 2013 The Royal Society of Chemistry. (c) The UV-vis spectrum of the obtained g-C_3N_4QDs. Inset: the photographs under illumination of white (left) and UV (365 nm, right) light. Reprinted with permission from ref. 83, Copyright 2015 Elsevier B.V., and (d) UV-vis absorption spectrum (red) of the g-C_3N_4QDs and FL spectra of g-C_3N_4QDs with the excitation wavelength at 330 nm to 460 nm. Inset: photographs of g-C_3N_4QDs under visible light (left) and 365 nm UV light (right). Reprinted with permission from ref. 72, Copyright 2015 The Royal Society of Chemistry.

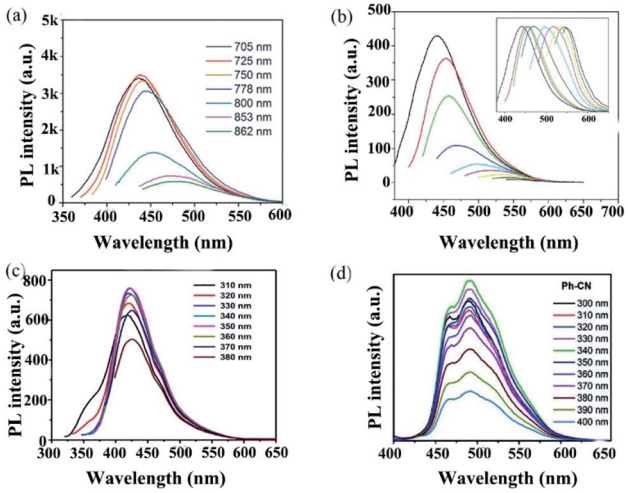

Fig. 14 (a) The upconversion PL spectra of the g-C_3N_4QDs. Reprinted with permission from ref. 28. Copyright 2014 The Royal Society of Chemistry. (b) PL emission spectra (with progressively longer excitation wavelengths from 360 to 540 nm on the left in 20 nm increments) of the g-C_3N_4QD dispersion. Inset: the normalized PL emission spectra. Reprinted with permission from ref. 88. Copyright 2011 The Royal Society of Chemistry. (c) PL spectra of g-C_3N_4QDs at different excitation wavelengths. Reprinted with permission from ref. 45. Copyright 2017 Elsevier B.V., and (d) PL spectra of colloidal g-C_3N_4QDs upon excitation at wavelengths from 300 to 400 nm. Reprinted with permission from ref. 58. Copyright 2016 Wiley-VCH Verlag GmbH & Co. KGaA, Weinheim.

the PL emission wavelength of g-C_3N_4QDs is longer than the excitation length, which follows the typical Stokes type emission. Despite the frequent demonstration of PL emissions of g-C_3N_4QDs in the literature, the relevant PL mechanism is still not clear. It is commonly suggested that the origin of the PL of g-C_3N_4QDs is attributed to the optical selectivity of different sized nanoparticles (quantum effect), emissive traps on the surface including defects, surface groups, and surface states. Unfortunately, systematic investigations on the influences of nanoparticle sizes, various surface groups, defects, and surface states on the PL properties of g-C_3N_4QDs are absent so far.

First, the PL emission of g-C_3N_4QDs is found to be dependent on the excitation wavelength, similar to that of carbon-based QDs (Fig. 14).[28,41,46,72,80,81,83,85,88] In most cases, the PL emission wavelength of g-C_3N_4QDs prepared by different methods is red-shifted with regard to the excitation wavelength and the emission intensity also varies with the increase of the excitation wavelength (Fig. 14b). For example, Sun's group reported that fluorescent g-C_3N_4QDs fabricated by the polymerization of CCl_4 and 1,2-ethylenediamine show excitation wavelength-dependent PL emission from 430 to 550 nm with the excitation wavelengths ranging from 360 to 540 nm.[88] This excitation wavelength-dependent PL behavior was also observed by other groups for g-C_3N_4QDs synthesized by different approaches.[47,65,72,73] It is worth noting that an excitation wavelength-independent feature was revealed for g-C_3N_4QDs in a few studies (Fig. 14c and d). Cui *et al.*[58] and Han *et al.*[45] observed that the intensity of PL emission changed but the

emission wavelength remained unchanged when the excitation wavelength increased from 300 to 400 nm or from 310 to 380 nm for phenyl-modified g-C_3N_4QDs and g-C_3N_4QDs, respectively. Secondly, g-C_3N_4QDs demonstrate a pH-dependent PL feature and the pH environment has different impacts on the PL emission (mainly the fluorescence intensity) of g-C_3N_4QDs prepared by different methods (Fig. 15).[41,46,72,80,87,88] Barman and Sadhukhan discovered that the PL emission wavelength remained unchanged while the fluorescence intensity of their g-C_3N_4QDs obtained from a microwave mediated method decreased with increasing solution pH from 2 to 13 (Fig. 15a), which implied that acidic sites were responsible for the PL emission of their g-C_3N_4QDs.[82] However, the g-C_3N_4QDs prepared by Hu *et al.* using a facile hydrothermal method displayed stronger PL intensity with the increase of solution pH, accompanied by a subtle blue shift under alkaline conditions (Fig. 15b).[46] Such pH sensitivity may be ascribed to the presence of nitrogen atoms containing lone-pair electrons which can be protonated at low pH, partly deactivating the PL emission state of the g-C_3N_4QDs, which is restored at high pH, resulting in the recovery of fluorescence. In addition, several studies found that the PL intensity first increased with the pH but then decreased with the further rising of pH (Fig. 15c).[42,53,58,88] Surprisingly, it was observed that oxygen and sulfur co-doped g-C_3N_4QDs exhibited a stable PL emission in a pH range from 5 to 9 (Fig. 15d),[43] revealing that the PL properties of g-C_3N_4QDs can also be tuned by heteroatom doping.

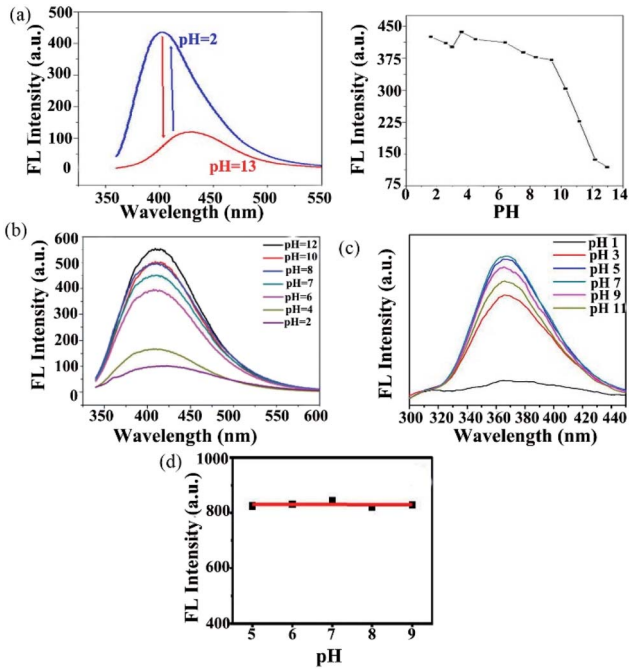

Fig. 15 (a) Left: pH dependent fluorescence spectra of g-C_3N_4QDs displaying the change of fluorescence intensity when pH is switched between 2 and 13, and right: plot of fluorescence intensity *vs.* pH of the medium (excitation wavelength = 340 nm). Reprinted with permission from ref. 82. Copyright 2012 The Royal Society of Chemistry. (b) pH-dependent PL intensity of g-C_3N_4QD aqueous solution. Reprinted with permission from ref. 46. Copyright 2017 The Royal Society of Chemistry. (c) Florescence spectra of g-C_3N_4QD solution under different pH conditions. Reprinted with permission from ref. 53. Copyright 2016 Wiley-VCH Verlag GmbH & Co. KGaA, Weinheim. (d) PL intensities of g-C_3N_4QDs at different pH values. Reprinted with permission from ref. 43. Copyright 2015 The Royal Society of Chemistry.

3.3 Upconversion PL (UCPL)

Upconversion is a phenomenon that simultaneous or sequential absorption of two or more photons with lower energy leads to the generation of higher-energy photons, *i.e.*, the excitation wavelength is longer than the emission wavelength.[97] Several studies show that g-C_3N_4QDs present the UPCL emission feature. Wang *et al.*[28] used long-wavelength light (705–862 nm) to excite g-C_3N_4QDs obtained from a hydrothermal cutting process and observed luminescence in the range of 350 to 600 nm with the strongest emission at 440 nm (Fig. 14a), indicating that g-C_3N_4QDs possess UCPL properties. The authors attributed the upconversion emission to the multiphonon active process. Yang *et al.*[38] also observed that irradiating g-C_3N_4QDs with near infrared light (700 to 820 nm) generated the emission of visible light (350 to 600 nm) with the strongest emission at 450 nm, which confirmed the UCPL feature of g-C_3N_4QDs. Currently, two possible mechanisms have been postulated for the upconversion emission: the multiphoton active process and anti-Stokes photoluminescence. Several researchers attributed the upconversion emission of g-C_3N_4QDs to the multiphoton active process owing to the reason that the energy difference between the excitation light and the emission light in the upconversion process is not a fixed value.[98] However, more solid proof should be provided in future to fully understand the intrinsic mechanisms.

3.4 Chemiluminescence (CL)

CL is the product of electromagnetic radiation by a chemical reaction between at least two reagents, in which an obtained electronically excited intermediate or product is subsequently relaxed to the ground state with the further emission of light. With the outstanding advantages of simple instrumentation, excellent sensitivity, being undisturbed by background scattered light, and automatic and versatile determination of a wide variety of species, CL has turned out to be a potential tool in analytical fields over the past few decades.[99–101] There are some different CL applications for g-C_3N_4QDs synthesized by different preparation methods. Several studies show that g-C_3N_4QDs have the characteristics of CL and thus can be applied for the detection of specific substances like free chlorine, metal ions, and so on. For instance, Lv *et al.* reported that the addition of NaClO solution to a g-C_3N_4QD suspension gave rise to a strong CL emission which was red-shifted compared to the PL of g-C_3N_4QDs (Fig. 16a and b), suggesting that such QDs exhibit promising applications for the detection of free chlorine in water.[81] The CL mechanism involved in the g-C_3N_4QDs–NaClO system is attributed to the following two reasons (Fig. 16c): (i) g-C_3N_4QDs can accept holes from the strongly oxidizing NaClO because of their unique band structures and the QDs are thus converted to oxidized g-C_3N_4QDs (g-C_3N_4QDs$^{\bullet+}$), whereas the excited electrons in the high energy band of g-C_3N_4QDs$^{\bullet+}$

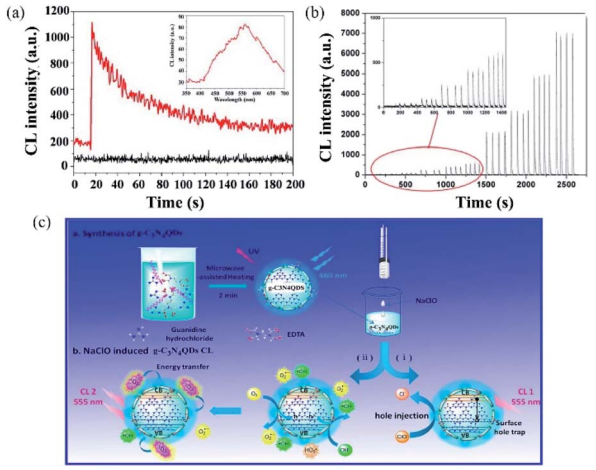

Fig. 16 (a) The CL kinetic file obtained when the NaClO solution was added into the control solution (guanidine hydrochloride or EDTA upon microwave treatment) (black line) and g-C_3N_4QD solution (red line). Conditions: the concentration of g-C_3N_4QDs and NaClO was 0.01 M and 1 μM. The inset shows the CL spectrum of the g-C_3N_4QDs–NaClO system obtained by using a fluorescence spectrometer with the xenon lamp turned off. (b) Flow injection signals for the determination of free chlorine concentration in the range from 2.0×10^{-8} to 1.0×10^{-5} M (various concentrations of chlorine: 0.02, 0.05, 0.1, 0.5, 1, 3, 5, 7, and 10 μM). Conditions: g-C_3N_4QDs with a concentration of 0.01 M. (c) Schematic illustration for the preparation of g-C_3N_4QDs and the CL mechanism of the g-C_3N_4QDs–NaClO system. Reprinted with permission from ref. 81. Copyright 2014 American Chemical Society.

recombine with the holes quickly, producing CL emission; (ii) singlet oxygen ($^1O_2$) or dimol singlet oxygen, which is evolved from the interactions between the as-formed reactive oxygen species in the g-C_3N_4QDs–NaClO system like $O_2^{\bullet-}$ that is produced by the reaction between g-C_3N_4QDs and oxygen (primarily coming from the decomposition of NaClO and a small fraction coming from the dissolved air in solution) and $^{\bullet}OH$ that originates from the oxidation of OH^- by g-C_3N_4QDs$^{\bullet+}$, can transfer energy to g-C_3N_4QDs to form excited-state g-C_3N_4QDs, and relaxation of such excited g-C_3N_4QDs also gives CL emission. In addition, Lv's group reported the applications of other g-C_3N_4QD-based CL systems including g-C_3N_4QDs–$K_3[Fe(CN)_6]$ system[72] and Ce(IV)–SO_3^{2-}–g-C_3N_4QD system[71] for the detection of divalent mercury and dopamine in water and iodide ions in urea samples, respectively.

3.5 Summary of the properties of g-C_3N_4QDs

The optical features of g-C_3N_4QDs are mainly resulted from the special size effect. g-C_3N_4QDs can act as photosensitizers in photo(electro)catalytic reactions due to their excellent light absorption performance. The peculiar PL and UCPL properties of g-C_3N_4QDs enable them to serve as spectral converters in photocatalysis, especially the UCPL behavior can result in the utilization of NIR light with longer wavelengths. The occurrence of PL of g-C_3N_4QDs is possibly attributed to the optical selectivity of differently sized nanodots (quantum effect), emissive traps on the surface including defects, surface groups, and surface states, yet further insight into the intrinsic PL mechanism is required. Meanwhile, the UCPL character is commonly suggested to have resulted from the multiphoton active process. With those optical features, photon utilization of g-C_3N_4QDs in photocatalysis is greatly extended. Regarding the CL emission of the g-C_3N_4QD-based system, it is caused by the returning of excited-state g-C_3N_4QDs that are induced by the electron and hole transfer between QDs and CL reagents to the ground-state QDs, during which energy and photons are produced. The CL characteristic of g-C_3N_4QDs can be adopted to the quick and intuitive detection of certain ions or special substances. Therefore, the unique properties of g-C_3N_4QDs spark their plentiful applications, especially in photocatalysis.

4. Applications in photocatalysis

As a semiconductor with optical absorption in the visible light region, g-C_3N_4QDs are usually employed as photosensitizers to combine with many traditional wide-gap photocatalysts which can only be activated by UV light, in order to enhance the efficiency of solar light for photocatalytic performances. The good water solubility[80] and chemical stability[47] of g-C_3N_4QDs can facilitate the large-scale fabrication of g-C_3N_4QD-based composite materials. In addition, g-C_3N_4QDs are also coupled with visible-light-driven photocatalysts to further extend the spectral responsive range of the photocatalytic system to the NIR region because of the UPCL properties of g-C_3N_4QDs.[28] Notably, the conductive band (CB) potential of some semiconductors is close to or higher than that of $O_2/^{\bullet}O_2^-$, which is unbeneficial to the production of $^{\bullet}O_2^-$, a reactive species during the photocatalytic process. In this respect, construction of g-C_3N_4QD-based composite photocatalysts can improve the production of $^{\bullet}O_2^-$ and boost the photocatalysis owing to the much more negative CB potential of g-C_3N_4QDs.[37,76] Furthermore, the heterojunctions formed between g-C_3N_4QDs and other semiconductors in the composites are able to slow down the recombination of electrons and holes and increase the charge separation efficiency, because the photoinduced g-C_3N_4QDs can act as both good electron donors and acceptors.[35] Owing to these multiple effects, the construction of compounds of g-C_3N_4QDs as photocatalysts is an effective way to boost the photocatalytic reactions. So far, various g-C_3N_4QD-based composite photocatalysts have been prepared and applied for hydrogen evolution,[28,34] photoelectrochemical sensing,[39,40] solar cells,[38] and degrading organic pollutants.[35–37] In this section, we mainly discuss their applications in the degradation of organic pollutants.

TiO_2 is one of the most popular photocatalysts owing to its good stability, low cost, efficient charge transfer, and non-toxicity. However, the wide band gap of TiO_2 (band gap = 3.0–3.2 eV) that is mostly photoactive under UV irradiation limits its promising application in photocatalysis. To address this issue, attempts to construct g-C_3N_4QDs/TiO_2 composites for eliminating organic contaminations were made. Lv *et al.*[37] fabricated a series of hybrid photocatalysts composed of Z-scheme rutile TiO_2 (rTiO_2) loaded with different amounts of g-C_3N_4QDs (g-C_3N_4QDs–rTiO_2) for visible-light-driven photocatalytic degradation of Rhodamine B (RhB) and oxidation of NO (Fig. 17).

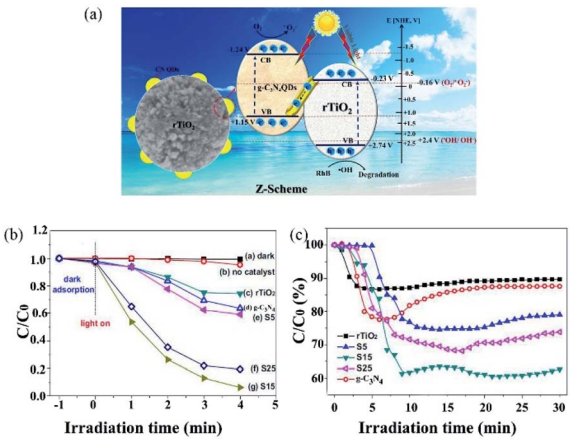

Fig. 17 (a) Photocatalytic removal mechanism of RhB and NO by the g-C_3N_4QDs–rTiO_2 photocatalyst under visible-light irradiation. (b) Photocatalytic degradation profiles of RhB by a series of g-C_3N_4QDs–rTiO_2 catalysts with different loadings of g-C_3N_4QDs (the molar ratios between g-C_3N_4QDs and rTiO_2 of 0.05 : 1, 0.15 : 1, and 0.25 : 1 were named S5, S15, and S25, respectively). (c) Comparison of the photocatalytic NO removal efficiencies in a single-pass flow of air over different g-C_3N_4QDs–rTiO_2 photocatalysts under visible-light irradiation. Reprinted with permission from ref. 37. Copyright 2016 Elsevier B.V.

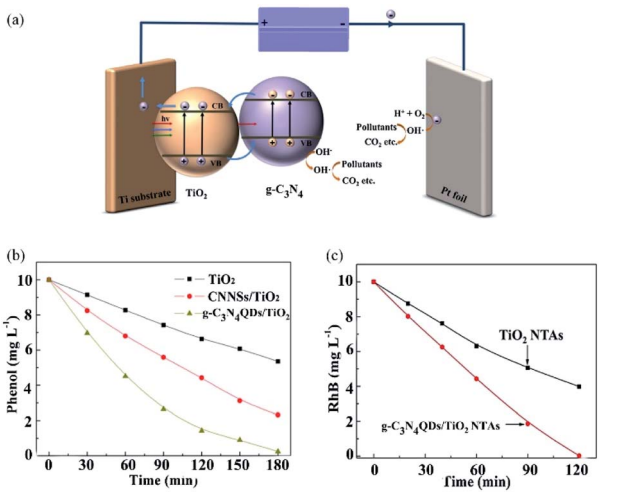

Fig. 18 (a) Schematic illustration of charge separation and pollutant degradation processes using g-C_3N_4QDs/TiO_2 NTA photoanodes under solar light. (b) Photoelectrochemical (PEC) degradation of phenol using TiO_2, g-C_3N_4 nanosheets/TiO_2 (CNNSs/TiO_2) and g-C_3N_4QDs/TiO_2 NTAs. (c) PEC degradation of RhB using TiO_2 and g-C_3N_4QDs/TiO_2 NTA photoelectrodes. Reprinted with permission from ref. 76. Copyright 2016 Elsevier B.V.

With these hybrid catalysts, much higher removal efficiencies of RhB and NO were achieved with respect to pure g-C_3N_4 and rTiO_2 and the sample with a nominal 15 at% QD loading showed the best photocatalytic performance among all the hybrid catalysts. As illustrated in Fig. 17a, the incorporation of g-C_3N_4QDs improves visible light harvesting ability and subsequently produces more photo-induced electrons and holes. Due to different CB and valence band (VB) edges between g-C_3N_4QDs and rTiO_2, photo-induced electrons are transferred from the CB of rTiO_2 to the VB of g-C_3N_4QDs, further excited to the CB of g-C_3N_4QDs, facilitating the separation of charge carriers. Meanwhile, the electrons in the CB of g-C_3N_4QDs and the holes in the VB of rTiO_2 react with the adsorbed oxidant (O_2) and reductant (OH^-/H_2O) respectively to generate $^{\bullet}OH$ and $^{\bullet}O_2^-$ radicals with a strong oxidizing ability, which are responsible for the subsequent oxidation of pollutants. In addition, several researchers reported the enhanced photocatalytic activity of g-C_3N_4QD modified TiO_2 NTAs as a membrane or electrode in degrading organic pollutants under visible light illumination.[34,55,67,76] Chen *et al.*[76] observed that nearly 100% removal of RhB and phenol was achieved under simulated solar light with a g-C_3N_4QDs/TiO_2 NTA photoanode in 120 min and 180 min, respectively, while only 50% of RhB and 30.1% of phenol were degraded by the TiO_2 NTA electrode under the same conditions. In the heterostructured g-C_3N_4QDs/TiO_2 NTA photocatalyst, g-C_3N_4QDs act as the photosensitizer to harvest visible phonons for improving the yield of charge carriers and the interfacial interaction between g-C_3N_4QDs and TiO_2 NTAs retards the electron–hole pair recombination, thereby enhancing the photocatalytic activity of the composite. Fig. 18a depicts the photocatalytic mechanism diagram of pollutant degradation over the g-C_3N_4QDs/TiO_2 NTA electrode. It can be seen that photogenerated electrons in the CB of g-C_3N_4QDs are first transported to the CB of TiO_2 NTAs and then to the negative electrode to generate $^{\bullet}OH$ for mineralizing pollutants, whereas photogenerated holes in the VB of g-C_3N_4QDs react with OH^-/H_2O to form $^{\bullet}OH$ and for oxidizing the pollutants.

Bismuth phosphate ($BiPO_4$) is a new oxy-acid salt photocatalyst with a wider band gap (3.85 eV) and higher photocatalytic activity compared to TiO_2. To broaden the exploitable spectrum of $BiPO_4$, Fang *et al.*[102] designed a novel composite architecture made up of g-C_3N_4QDs and $BiPO_4$ nanocrystals and tested its visible light-induced photocatalytic performance by selecting hazardous methylene orange (MO) as the target pollutant (Fig. 19). A degradation efficiency of 92% is achieved by the g-C_3N_4QDs/$BiPO_4$ composite in 180 min with a degradation rate constant k of 0.0135 min^{-1}, which is much higher than that achieved by $BiPO_4$ nanocrystals (less than 10%) and pure g-C_3N_4 (75%, 0.0079 min^{-1}). On one hand, the much higher specific surface area of the g-C_3N_4QDs/$BiPO_4$ composite (39.4 $m^2\ g^{-1}$) than that of pristine $BiPO_4$ nanocrystals (8.3 $m^2\ g^{-1}$) is beneficial for the adsorption of the pollutant onto the photocatalyst and the exposure of more active sites.[104] On the other hand, the heterojunctions formed between g-C_3N_4QDs and $BiPO_4$ nanocrystals significantly enhance the separation and transport of charge carriers in the composite catalyst. Such a g-C_3N_4QDs/$BiPO_4$ composite catalyst also possesses a good stability as shown in Fig. 19c.

Other than TiO_2, bismuth complex oxides have also been considered as potential candidates of photocatalysts in recent years since they can be photoactivated by visible light. Unluckily, these oxides suffer from low CB levels and insufficient visible light absorption.[105,106] To overcome the above drawbacks, several studies paid attention to the construction of

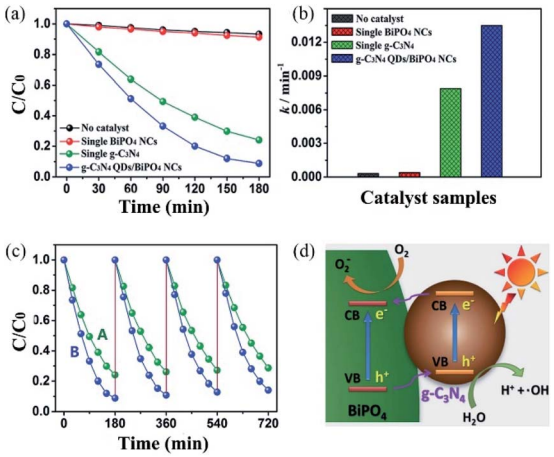

Fig. 19 (a) Photocatalytic activities and (b) corresponding rate constant k of MO degradation for g-C_3N_4QDs/$BiPO_4$, $BiPO_4$ and g-C_3N_4; (c) cycling runs of MO degradation on single g-C_3N_4 (curve A) and g-C_3N_4QDs/$BiPO_4$ (curve B) photocatalysts; (d) schematic diagram of the separation and transport of photogenerated electron–hole pairs at the g-C_3N_4QDs/$BiPO_4$ interface. Reprinted with permission from ref. 102. Copyright 2014 The Royal Society of Chemistry.

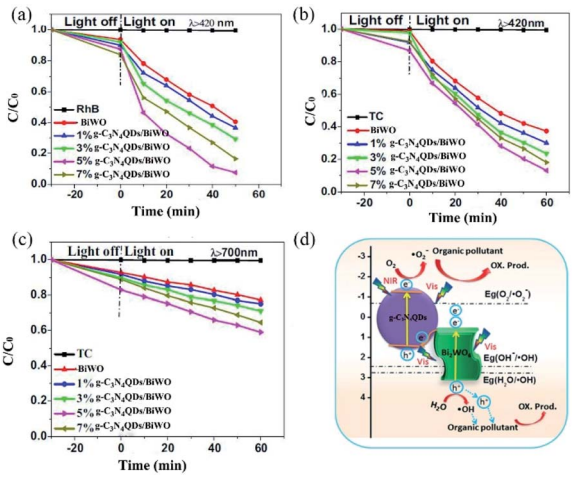

Fig. 20 Photocatalytic degradation of (a) RhB under visible light irradiation; (b) TC under visible light irradiation; (c) TC under near-infrared light irradiation with different g-C_3N_4QDs/BiWO photocatalysts; (d) a Z-scheme mechanism of the g-C_3N_4QDs/BiWO photocatalyst under wide spectrum light irradiation. Reprinted with permission from ref. 103. Copyright 2019 Elsevier Inc.

g-C_3N_4QDs/bismuth complex oxide composites like g-C_3N_4QDs/Bi_2WO_6 (g-C_3N_4QDs/BiWO), g-C_3N_4QDs/$Bi_2Ti_2O_7$, and g-C_3N_4QDs/$Bi_2Mo_2O_6$.[36,39,102,103,107] For example, Zhang *et al.*[103] developed a direct Z-scheme photocatalyst (g-C_3N_4QDs/BiWO) by loading g-C_3N_4QDs onto ultra-thin Bi_2WO_6 nanosheets for the elimination of RhB and tetracycline (TC) under broad spectrum light illumination. The authors found that loading of various amounts of g-C_3N_4QDs increased the photocatalytic activity of Bi_2WO_6 nanosheets toward the pollutant degradation under both visible light and NIR light irradiation, and the composite catalyst with a loading amount of 5 wt% g-C_3N_4QDs (5% g-C_3N_4QDs/BiWO) exhibited the best photocatalytic activity among all the samples (Fig. 20a and b). Particularly, the degradation efficiency of TC by 5% g-C_3N_4QDs/BiWO was around twice that by pure Bi_2WO_6 nanosheets under NIR light irradiation (Fig. 20c), attributable to the UCPL behavior of g-C_3N_4QDs. A Z-scheme mechanism of the photocatalytic degradation of organic pollutants over g-C_3N_4QDs/BiWO was proposed as shown in Fig. 20d. Under visible light illumination, photogenerated electrons in the CB of Bi_2WO_6 can be transferred to the highest occupied molecular orbital (HOMO) of g-C_3N_4QDs to inhibit the recombination of the photogenerated carriers, whilst the remaining electrons and holes in the lowest unoccupied molecular orbital (LUMO) of g-C_3N_4QDs and the VB of Bi_2WO_6 could help to form reactive oxygen species ($^{\bullet}OH$ and $^{\bullet}O_2^-$) to attack organic pollutants. In addition, holes in the VB of Bi_2WO_6 can also oxidize the organics directly due to the high VB edge of Bi_2WO_6. With the improved charge separation efficiency, more electrons and holes are accumulated in the composite and subsequently generate more reactive species, hence leading to the enhanced removal of organic pollutants. Under NIR light irradiation, g-C_3N_4QDs serve as a spectral converter to generate visible light emission, taking advantage of their UPCL features. Subsequently, a similar photocatalytic degradation process to that under visible light irradiation occurred.

Besides the aforementioned binary g-C_3N_4QD-based composite catalysts, ternary compounds involving g-C_3N_4QDs have also been assembled to obtain high-performance photocatalysts. In the ternary compound system, there are at least two contact interfaces, which enable the separation of photogenerated electrons and holes more efficiently and further boost the photocatalytic performance. A few examples demonstrated the improved photocatalytic degradation of organic pollutants with g-C_3N_4QD-based ternary compounds.[35,36] Che *et al.*[35] assembled g-C_3N_4QDs on the surface of leaf-like $InVO_4$/$BiVO_4$ nanocrystals (g-C_3N_4QDs/$InVO_4$/$BiVO_4$) and investigated the photocatalytic activity of the as-prepared composite photocatalyst toward RhB degradation. As shown in Fig. 21, g-C_3N_4QDs/$InVO_4$/$BiVO_4$ is more photoactive than all one-component and two-component samples and it achieves a ~100% removal of RhB in 40 min under visible light irradiation (Fig. 21a). The noticeable decrease of the PL intensity of g-C_3N_4QDs/$InVO_4$/$BiVO_4$ (Fig. 21b) reveals that the photoinduced electrons in the CB of g-C_3N_4QDs can be transferred to $InVO_4$ and then to $BiVO_4$ or directly moved to $BiVO_4$, and photoinduced holes in the VB of $BiVO_4$ are transported to g-C_3N_4QDs straightly or *via* two steps, which effectively suppress the recombination of photogenerated electrons and holes in the ternary system and thus improve the photocatalytic activity. Fig. 21c describes the possible pathways of the separation and migration of photogenerated carriers in the ternary compound. Because the VB potential of $BiVO_4$ is slightly higher than that of $OH^-/^{\bullet}OH$, it is difficult to generate $^{\bullet}OH$ radicals for degrading organic pollutants with the g-C_3N_4QDs/$InVO_4$/$BiVO_4$ photocatalyst, which is consistent with the results of quenching

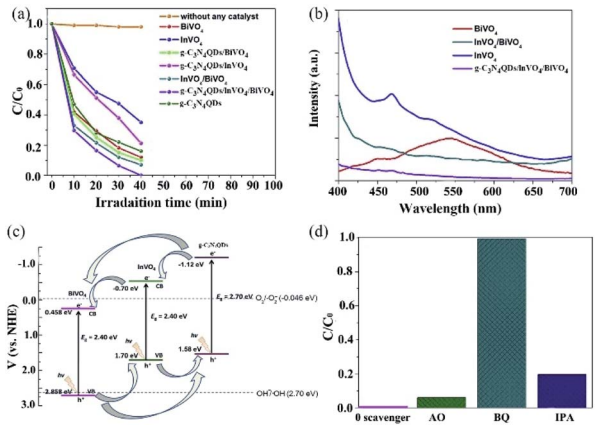

Fig. 21 (a) Photodegradation efficiencies of RhB as a function of irradiation time for different photocatalysts. (b) Room temperature PL spectra of the as-synthesized samples under an excitation wavelength of 325 nm. (c) Schematic diagram of the separation and transfer of photogenerated charges in the ternary heterostructure under visible light irradiation. (d) Trapping experiment of active species during the photocatalytic degradation of RhB over the g-C_3N_4QDs/$InVO_4$/$BiVO_4$ sample under visible light irradiation. Reprinted with permission from ref. 35. Copyright 2016 Elsevier B.V.

experiments (Fig. 21d), showing that $^{\bullet}O_2^-$ radicals are the main reactive species involved in the photocatalytic reactions.

Later, Chang *et al.*[36] further proved that g-C_3N_4QD-based ternary composite photocatalysts were more efficient than the corresponding binary composite systems in their work on nanoheterostructured Bi_2MoO_6 nanosheets deposited with Ag and g-C_3N_4QDs. As shown in Fig. 22a, the as-prepared g-C_3N_4QDs/Ag/Bi_2MoO_6 composite shows a 100% removal of RhB

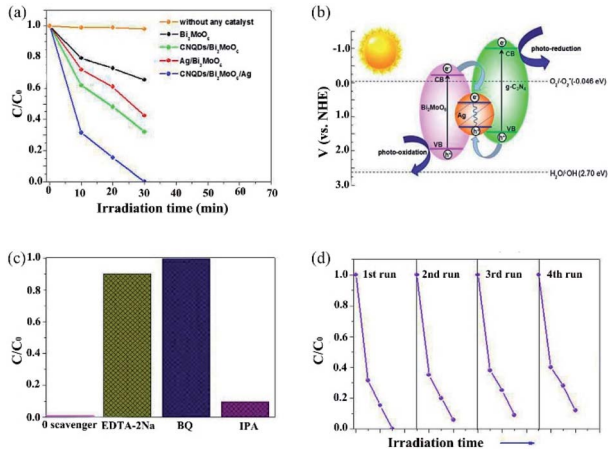

Fig. 22 (a) Photodegradation efficiencies of RhB as a function of irradiation time for different photocatalysts. (b) Photocatalytic mechanism scheme of the g-C_3N_4QDs/Ag/Bi_2MoO_6 composite under visible light irradiation (λ > 420 nm). (c) Trapping experiments of active species during the photocatalytic degradation of RhB over the g-C_3N_4QDs/Ag/Bi_2MoO_6 sample under visible light irradiation. (d) Cycling runs for the photocatalytic degradation of RhB over the g-C_3N_4QDs/Ag/Bi_2MoO_6 sample under visible light irradiation. Reprinted with permission from ref. 36. Copyright 2017 Elsevier B.V.

in 30 min under visible light irradiation, much higher compared with pure Bi_2MoO_6, Ag/Bi_2MoO_6 and g-C_3N_4QDs/Bi_2MoO_6. For this ternary compound, g-C_3N_4QDs and Bi_2MoO_6 mainly act as photosensitizers to absorb visible light, and Ag serves as the electron-conduction bridge due to its small band-gap to accept electrons from the CB of Bi_2MoO_6 and holes from the VB of g-C_3N_4QDs (Fig. 22b). In this way, the separation of photoinduced electrons and holes in both g-C_3N_4QDs and Bi_2MoO_6 is remarkably accelerated during photocatalysis, further promoting the degradation of RhB. In addition, the surface plasmon resonance of Ag can enhance the visible light absorption of the composite, which was beneficial for the photocatalytic reaction.

Furthermore, the integration of g-C_3N_4QDs with other types of semiconductors other than the above semiconducting metal oxide as photocatalysts for organic pollutant remediation can also be found in the literature. Yuan *et al.*[56] reported the photocatalytic performance of a composite containing ultrathin g-C_3N_4 sheets embedded with g-C_3N_4QDs (g-C_3N_4QDs-utg-C_3N_4) and Sb_2S_3 upon NIR irradiation. Sb_2S_3 has a suitable band gap that covers both the visible and NIR regions of the solar spectrum,[108] while the intrinsic low photoelectric conversion efficiency limits its practical application. Due to the peculiar photoinduced electron transfer properties of g-C_3N_4 sheets and QDs, the integration of Sb_2S_3 with g-C_3N_4 sheets and QDs is an effective strategy to improve the photocatalytic activity of Sb_2S_3. Fig. 23a–c demonstrate that g-C_3N_4QD composites with different loadings of g-C_3N_4QDs-utg-C_3N_4 (the as-prepared g-C_3N_4QD samples with an expected g-C_3N_4QDs-utg-C_3N_4 volume of 10, 35 and 50 ml were labeled CNS-1, CNS-3, and CNS-5, respectively.) exhibit enhanced photocatalytic performance toward methyl orange (MO) under light illumination spanning from the UV to the NIR region compared to Sb_2S_3. By optimizing the loading amount of g-C_3N_4QDs-utg-C_3N_4, the CNS-3 sample can even realize 70% removal of MO under NIR irradiation in 120 min, attributed to the UCPL properties of g-C_3N_4QDs. In addition, the higher photocurrent response of CNS-3 than Sb_2S_3 under UV, visible light and NIR illumination confirms that the electron transfer and charge carrier separation are improved, which leads to better photocatalytic activity. A schematic illustration of photocatalytic degradation of MO on the CNS composite under NIR illumination is shown in Fig. 23e. As seen, g-C_3N_4QDs are the main spectral converter and absorb NIR light and convert it to shorter wavelength light, subsequently producing electrons and holes. The electrons are injected from the CB of g-C_3N_4 to that of Sb_2S_3 while the holes left in the VB of Sb_2S_3 are transferred to that of g-C_3N_4, hindering the recombination of the carriers. Afterwards, MO is decomposed by the separated holes and $^{\bullet}O_2^-$ produced from the reaction between excited electrons and the O_2 adsorbed on the surface of Sb_2S_3, which can be supported by the results of radical scavenging experiments (Fig. 23d).

An enhanced photoelectrocatalytic activity of a photocathode composed of Si nanowires (SiNWs) coated with g-C_3N_4QDs (SiNWs@g-C_3N_4QDs) towards the degradation of 4-chlorophenol was reported by Yu *et al.*[54] In order to prevent the easy passivation of Si nanowires in aqueous solution, the authors

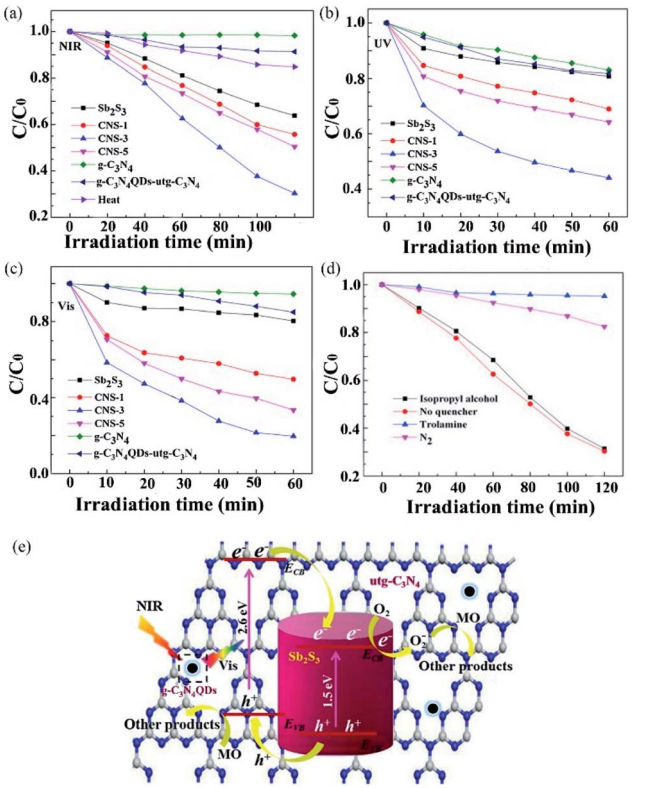

Fig. 23 (a) MO degradation photocatalytic performance of g-C_3N_4QDs-utg-C_3N_4 under near-infrared (NIR), (b) ultraviolet (UV), and (c) visible (Vis) irradiation. (d) Proposed mechanism for the MO degradation on the g-C_3N_4QD composites under NIR irradiation. (e) Effect of different reactive species scavengers on MO photodegradation by CNS-3 under NIR irradiation. Reprinted with permission from ref. 56. Copyright 2016 Elsevier B.V.

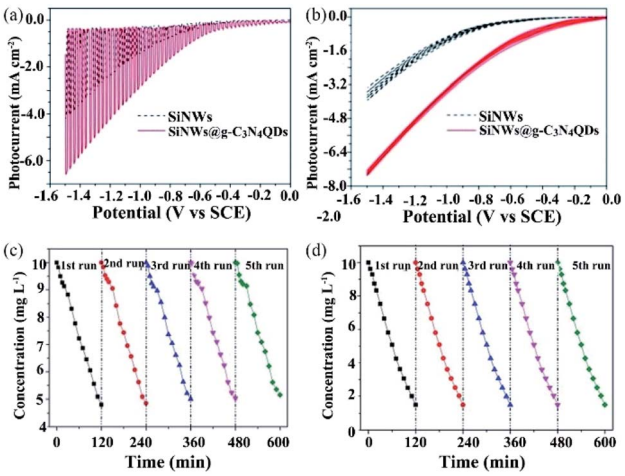

Fig. 24 (a) *I–V* curves of SiNW and SiNWs@g-C_3N_4QD photocathodes and (b) 10 cycles of cyclic voltammetry curves of SiNW and SiNWs@g-C_3N_4QD photocathodes in 0.5 M H_2SO_4 solution under xenon lamp illumination (100 mW cm^{-2}). Consecutive runs of the photoelectrocatalytic degradation of 4-chlorophenol ($C_0 = 10$ mg L^{-1}) with the (c) SiNW photocathode and (d) SiNWs@g-C_3N_4QD photocathode (−1.2 V *vs.* SCE) under visible light irradiation ($\lambda > 400$ nm, $I = 100$ mW cm^{-2}). Reprinted with permission from ref. 54. Copyright 2017 The Royal Society of Chemistry.

used g-C_3N_4QDs as a protection material to wrap the Si nanowires due to their superior photocorrosion resistance. Additionally, the unique optical absorption and electronic properties of g-C_3N_4QDs favor the photoelectrochemical process. As evidenced by the photocurrent curves in Fig. 24a, the photocurrent of SiNWs@g-C_3N_4QDs is much higher than that of SiNWs, attributable to the heterojunction formed between the SiNWs and g-C_3N_4QDs that can facilitate the electron transfer. A degradation efficiency of 85.1% for 4-chlorophenol is achieved with the SiNWs@g-C_3N_4QD photocathode, higher than that achieved with the SiNW photocathode (52.0%). Furthermore, a better photoelectrocatalytic stability is exhibited by the SiNWs@g-C_3N_4QD electrode compared to the SiNW electrode (Fig. 24b–d), proving that g-C_3N_4QDs act effectively as a protective layer.

Therefore, g-C_3N_4QDs play an important role in photocatalytic and photoelectrocatalytic degradation of pollutants as a photosensitizer, spectral converter (sp-converter) and photostabilizer to prevent photocorrosion (Fig. 25). For example, by combining traditional wide-gap photocatalysts, the composites (*e.g.* g-C_3N_4QDs/TiO_2, g-C_3N_4QDs/bismuth complex oxides, *etc.*) not only absorb ultraviolet light but also expand the light adsorption to the visible region, improving the utilization of photons. In addition, g-C_3N_4QDs can be used as a sp-converter in the photocatalytic process due to the effect of UCPL. The combination of g-C_3N_4QDs and certain semiconductors, like Sb_2S_3 semiconductors, exhibits enhanced photocatalytic performance under light illumination spanning from the UV to the NIR region. Interestingly, g-C_3N_4QDs also have excellent photocorrosion resistance to prevent photocatalysts from being passivated during photoelectrocatalytic reactions and improve the photoelectrocatalytic performance. Definitely, there are still many potential applications for g-C_3N_4QDs in the fields of

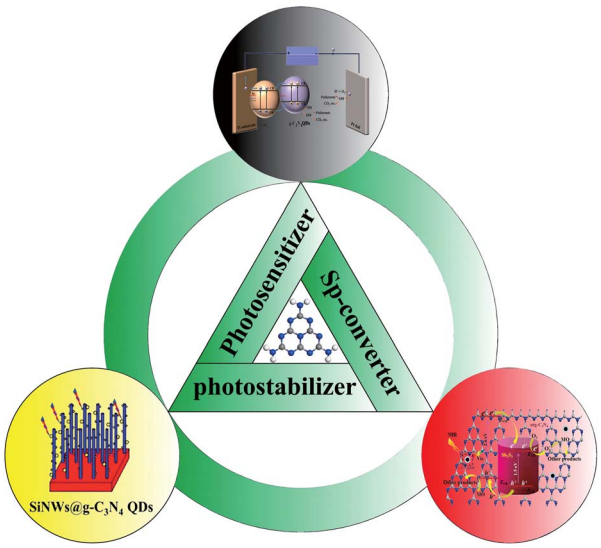

Fig. 25 The role of g-C_3N_4QDs in photocatalytic and photoelectrocatalytic degradation of pollutants.

photocatalysis and photoelectrocatalysis. It is hoped that g-C_3N_4QDs can be further explored for application in relevant fields by summarizing the studies of pre-existing photocatalysis by g-C_3N_4QDs here.

5. Summary and outlook

The unique optical properties, electronic structures, good water solubility and biocompatibility of g-C_3N_4QDs have stimulated the research on their synthesis, modifications and applications. g-C_3N_4QDs prepared by different methods show varying characteristics, enabling them to be widely applied in bio-imaging, ion detection, energy storage and conversion, and environmental remediation. To date, a diversity of simple, low-cost and size-controllable methods have been developed for the fabrication of g-C_3N_4QDs with different physicochemical properties. These methods are grouped into two major synthetic strategies, *i.e.* top-down strategy and bottom-up strategy. The top-down strategy primarily includes the sonication method, hydrothermal method and other methods, while the bottom-up strategy involves the solid-phase method, microwave-assisted solvothermal method and quasi-CVD method. The g-C_3N_4QDs prepared by these methods exhibit effective absorption of light, tunable PL and special UCPL. Those excellent optical properties make g-C_3N_4QDs competent for photon utilization under a wide range of wavelengths (from UV to IR). Therefore, g-C_3N_4QDs are used as a multifunctional material during photocatalytic reactions. For example, as a photosensitizer, they can be combined with a wide-bandgap semiconductor to greatly improve the photon utilization during photocatalysis processes. In addition, it can also be used as a converter to extend the spectral utilization of the photocatalyst to the NIR region. Interestingly, due to the good stability of g-C_3N_4QDs, they show the ability of preventing photocorrosion in photoelectrocatalytic processes.

Although remarkable progress has been made in this field, there are still many issues that need to be addressed:

(i) Methods for large scale synthesis of g-C_3N_4QDs are still unavailable. Among the diverse routes, the solid phase method appears to be the most promising one to be scaled up, but the yield of this method needs to be further enhanced to reduce the dialysis post-treatment time and optimization of the experimental parameters for size-controlled synthesis is of necessity. Therefore, efforts on the mass production of g-C_3N_4QDs with good quality and uniform size in future are urgent.

(ii) Available approaches to accurately engineer the number of defects in g-C_3N_4QDs are still lacking, while the defects of g-C_3N_4QDs have an important influence on their optical and electronic properties. Consequently, more attention should be paid to the well-defined structural synthesis of g-C_3N_4QDs.

(iii) Surface modifications of g-C_3N_4QDs can also affect their electronic and photocatalytic properties, but relevant studies are limited so far. For example, several studies demonstrated that doping g-C_3N_4QDs with heteroelements like sulfur, phosphorus, fluorine, and boron could improve the optical properties, while the effect of doping on the photocatalytic properties of g-C_3N_4QDs is unknown. In addition, the properties of g-C_3N_4QDs may be changed owing to the type and number of surface functional groups and defects. Hence, simple and controllable functionalization and doping of g-C_3N_4QDs for better PL control and higher efficiency for many applications are extremely desirable in future.

(iv) Further theoretical and experimental studies on the mechanisms of g-C_3N_4QD-related properties are necessary in order to achieve a full utilization of their specific properties. For instance, theoretical calculations on the influences of defects, functional groups and doping on the band structure and photocatalytic properties of g-C_3N_4QDs are helpful for the controllable synthesis of high-performance g-C_3N_4QDs. Meanwhile, modelling of g-C_3N_4QD-based composites is essential for further understanding the role of g-C_3N_4QDs in the photocatalytic process and the reaction process, such as the electron distribution in g-C_3N_4QD composites before and after the photo-activation. By combining the calculation with experimental results, insight into the photocatalytic activation processes can be gained.

(v) In view of the good photocatalytic performances of g-C_3N_4QD-based composite photocatalysts in the removal of aqueous organic pollutants, these composite photocatalysts can also be applied for the elimination of pollutants in air (*e.g.* volatile organic compounds, NO, SO_2, H_2S, *etc.*) which is also one of the major environmental problems around the world. Unfortunately, related research has rarely been reported. Thus, more efforts should be devoted to the applications of g-C_3N_4QD-based composite photocatalysts in air purification.

Overall, many challenges and opportunities are waiting for researchers to explore the huge potential of g-C_3N_4QDs in various areas in the future. We wish that this review is able to offer clues on the rational design of g-C_3N_4QD-based photocatalysts in order to achieve efficient and long-term stable photocatalysts for practical applications.

Conflicts of interest

There are no conflicts to declare.

Acknowledgements

This work was supported by the National Natural Science Foundation of China (No. 21607029, 21777033, 21806024 and 41425015), China Postdoctoral Science Foundation (No. 2017M622637), Science and Technology Planning Project of Guangdong Province (No. 2017B020216003), and Innovation Team Project of Guangdong Provincial Department of Education (No. 2017KCXTD012).

References

1 A. J. Bard, *Science*, 1980, **207**, 139.
2 A. Kudo and Y. Miseki, *Chem. Soc. Rev.*, 2009, **38**, 253–278.
3 G. Liu, X. Li, J. Zhao, H. Hidaka and N. Serpone, *Environ. Sci. Technol.*, 2000, **34**, 3982–3990.
4 G. Li, X. Nie, Y. Gao and T. An, *Appl. Catal., B*, 2016, **180**, 726–732.

5 M. Wu, H. Lv, T. Wang, Z. Ao, H. Sun, C. Wang, T. An and S. Wang, *Catal. Today*, 2018, **315**, 205–212.
6 Y. Zhou, G. Cheng, K. Chen, J. Lu, J. Lei and S. Pu, *Ecotoxicol. Environ. Saf.*, 2019, **170**, 278–285.
7 M. Wu, X. He, B. Jing, T. Wang, C. Wang, Y. Qin, Z. Ao, S. Wang and T. An, *J. Hazard. Mater.*, 2020, **384**, 121323.
8 J. C. Yu, W. Ho, J. Yu, H. Yip, P. K. Wong and J. Zhao, *Environ. Sci. Technol.*, 2005, **39**, 1175–1179.
9 W. Wang, G. Li, D. Xia, T. An, H. Zhao and P. Wong, *Environ. Sci.: Nano*, 2017, **4**, 782–799.
10 G. Li, X. Nie, J. Chen, Q. Jiang, T. An, P. K. Wong, H. Zhang, H. Zhao and H. Yamashita, *Water Res.*, 2015, **86**, 17–24.
11 W. Wang, T. An, G. Li, D. Xia, H. Zhao, J. C. Yu and P. K. Wong, *Appl. Catal., B*, 2017, **217**, 570–580.
12 S. N. Habisreutinger, L. Schmidt-Mende and J. K. Stolarczyk, *Angew. Chem., Int. Ed.*, 2013, **52**, 7372–7408.
13 X. Wang, F. Wang, Y. Sang and H. Liu, *Adv. Energy Mater.*, 2017, **7**, 1700473.
14 S.-P. Wu, X.-Z. Dai, J.-R. Kan, F.-D. Shilong and M.-Y. Zhu, *Chin. Chem. Lett.*, 2017, **28**, 625–632.
15 Y. Zhu, Z.-S. Bai and H.-L. Wang, *Chin. Chem. Lett.*, 2017, **28**, 633–641.
16 D. M. Schultz and T. P. Yoon, *Science*, 2014, **343**, 1239176.
17 F. Goettmann, A. Fischer, M. Antonietti and A. Thomas, *Angew. Chem., Int. Ed.*, 2006, **45**, 4467–4471.
18 X. Wang, K. Maeda, X. Chen, K. Takanabe, K. Domen, Y. Hou, X. Fu and M. Antonietti, *J. Am. Chem. Soc.*, 2009, **131**, 1680–1681.
19 S. Cao, J. Low, J. Yu and M. Jaroniec, *Adv. Mater.*, 2015, **27**, 2150–2176.
20 J. Liebig, *Ann. Pharm.*, 1834, **10**, 1–47.
21 S. Patnaik, S. Martha and K. M. Parida, *RSC Adv.*, 2016, **6**, 46929–46951.
22 P. Niu, L. Zhang, G. Liu and H.-M. Cheng, *Adv. Funct. Mater.*, 2012, **22**, 4763–4770.
23 K. Maeda, X. Wang, Y. Nishihara, D. Lu, M. Antonietti and K. Domen, *J. Phys. Chem. C*, 2009, **113**, 4940–4947.
24 S. C. Yan, Z. S. Li and Z. G. Zou, *Langmuir*, 2009, **25**, 10397–10401.
25 F. Dong, Z. Wang, Y. Sun, W.-K. Ho and H. Zhang, *J. Colloid Interface Sci.*, 2013, **401**, 70–79.
26 A. Thomas, A. Fischer, F. Goettmann, M. Antonietti, J.-O. Müller, R. Schlögl and J. M. Carlsson, *J. Mater. Chem.*, 2008, **18**, 4893–4908.
27 Y. Zheng, J. Liu, J. Liang, M. Jaroniec and S. Z. Qiao, *Energy Environ. Sci.*, 2012, **5**, 6717–6731.
28 W. Wang, J. C. Yu, Z. Shen, D. K. Chan and T. Gu, *Chem. Commun.*, 2014, **50**, 10148–10150.
29 X.-H. Li, J. Zhang, X. Chen, A. Fischer, A. Thomas, M. Antonietti and X. Wang, *Chem. Mater.*, 2011, **23**, 4344–4348.
30 X. Wang, K. Maeda, X. Chen, K. Takanabe, K. Domen, Y. Hou, X. Fu and M. Antonietti, *J. Am. Chem. Soc.*, 2009, **131**, 1680–1681.
31 J. Sun, J. Zhang, M. Zhang, M. Antonietti, X. Fu and X. Wang, *Nat. Commun.*, 2012, **3**, 1139.
32 W. Wang, J. C. Yu, Z. Shen, D. K. L. Chan and T. Gu, *Chem. Commun.*, 2014, **50**, 10148–10150.
33 Z. Zhou, Y. Shen, Y. Li, A. Liu, S. Liu and Y. Zhang, *ACS Nano*, 2015, **9**, 12480–12487.
34 G. Li, Z. Lian, W. Wang, D. Zhang and H. Li, *Nano Energy*, 2016, **19**, 446–454.
35 X. Lin, D. Xu, J. Zheng, M. Song, G. Che, Y. Wang, Y. Yang, C. Liu, L. Zhao and L. Chang, *J. Alloys Compd.*, 2016, **688**, 891–898.
36 X. Lin, D. Xu, R. Zhao, Y. Xi, L. Zhao, M. Song, H. Zhai, G. Che and L. Chang, *Sep. Purif. Technol.*, 2017, **178**, 163–168.
37 Y. Li, K. Lv, W. Ho, F. Dong, X. Wu and Y. Xia, *Appl. Catal., B*, 2017, **202**, 611–619.
38 X. Chen, Q. Liu, Q. Wu, P. Du, J. Zhu, S. Dai and S. Yang, *Adv. Funct. Mater.*, 2016, **26**, 1719–1728.
39 S. Chen, N. Hao, D. Jiang, X. Zhang, Z. Zhou, Y. Zhang and K. Wang, *J. Electroanal. Chem.*, 2017, **787**, 66–71.
40 X. Pang, H. Bian, W. Wang, C. Liu, M. S. Khan, Q. Wang, J. Qi, Q. Wei and B. Du, *Biosens. Bioelectron.*, 2017, **91**, 456–464.
41 W. Guan, W. Gu, L. Ye, C. Guo, S. Su, P. Xu and M. Xue, *Int. J. Nanomed.*, 2014, **9**, 5071–5078.
42 H. Li, F.-Q. Shao, H. Huang, J.-J. Feng and A.-J. Wang, *Sens. Actuators, B*, 2016, **226**, 506–511.
43 Y.-C. Lu, J. Chen, A.-J. Wang, N. Bao, J.-J. Feng, W. Wang and L. Shao, *J. Am. Chem. Soc.*, 2015, **3**, 73–78.
44 N. Wang, H. Fan, J. Sun, Z. Han, J. Dong and S. Ai, *Carbon*, 2016, **109**, 141–148.
45 Y. Yin, Y. Zhang, T. Gao, T. Yao, J. Han, Z. Han, Z. Zhang, Q. Wu and B. Song, *Mater. Chem. Phys.*, 2017, **194**, 293–301.
46 Y. Zhan, Z. Liu, Q. Liu, D. Huang, Y. Wei, Y. Hu, X. Lian and C. Hu, *New J. Chem.*, 2017, **41**, 3930–3938.
47 X. Zhang, H. Wang, H. Wang, Q. Zhang, J. Xie, Y. Tian, J. Wang and Y. Xie, *Adv. Mater.*, 2014, **26**, 4438–4443.
48 S. Barman and M. Sadhukhan, *J. Mater. Chem.*, 2012, **22**, 21832–21837.
49 E. Z. Lee, Y. S. Jun, W. H. Hong, A. Thomas and M. M. Jin, *Angew. Chem., Int. Ed.*, 2010, **49**, 9706–9710.
50 C. Cheng, Y. Huang, X. Tian, B. Zheng, Y. Li, H. Yuan, D. Xiao, S. Xie and M. M. Choi, *Anal. Chem.*, 2012, **84**, 4754–4759.
51 E. Z. Lee, S. U. Lee, N. S. Heo, G. D. Stucky, Y. S. Jun and W. H. Hong, *Chem. Commun.*, 2012, **48**, 3942–3944.
52 X. Zhang, X. Xie, H. Wang, J. Zhang, B. Pan and Y. Xie, *J. Am. Chem. Soc.*, 2013, **135**, 18–21.
53 Z. Song, T. Lin, L. Lin, S. Lin, F. Fu, X. Wang and L. Guo, *Angew. Chem., Int. Ed. Engl.*, 2016, **55**, 2773–2777.
54 Y. Su, B. Sun, S. Chen, H. Yu and J. Liu, *RSC Adv.*, 2017, **7**, 14832–14836.
55 B. Sun, N. Lu, Y. Su, H. Yu, X. Meng and Z. Gao, *Appl. Surf. Sci.*, 2017, **394**, 479–487.
56 H. Wang, X. Yuan, H. Wang, X. Chen, Z. Wu, L. Jiang, W. Xiong and G. Zeng, *Appl. Catal., B*, 2016, **193**, 36–46.
57 X. Wang, L. Wang, F. Zhao, C. Hu, Y. Zhao, Z. Zhang, S. Chen, G. Shi and L. Qu, *Nanoscale*, 2015, **7**, 3035–3042.

58 Q. Cui, J. Xu, X. Wang, L. Li, M. Antonietti and M. Shalom, *Angew. Chem.*, 2016, **55**, 3672–3676.
59 Q. Fang, B. Li, Y.-Y. Li, W.-Q. Huang, W. Peng, X. Fan and G.-F. Huang, *Adv. Powder Technol.*, 2019, **30**, 1576–1583.
60 X. Pang, C. Cui, M. Su, Y. Wang, Q. Wei and W. Tan, *Nano Energy*, 2018, **46**, 101–109.
61 Q. Liu, D. Zhu, M. Guo, Y. Yu and Y. Cao, *Chin. Chem. Lett.*, 2019, **30**, 1639–1642.
62 A. Bandyopadhyay, D. Ghosh, N. M. Kaley and S. K. Pati, *J. Phys. Chem. C*, 2017, **121**, 1982–1989.
63 C.-Z. Li, Z.-B. Wang, X.-L. Sui, L.-M. Zhang and D.-M. Gu, *RSC Adv.*, 2016, **6**, 32290–32297.
64 X. Lin, D. Xu, J. Zheng, M. Song, G. Che, Y. Wang, Y. Yang, C. Liu, L. Zhao and L. Chang, *J. Alloys Compd.*, 2016, **688**, 891–898.
65 J. Wu, S. Yang, J. Li, Y. Yang, G. Wang, X. Bu, P. He, J. Sun, J. Yang, Y. Deng, G. Ding and X. Xie, *Adv. Opt. Mater.*, 2016, **4**, 2095–2101.
66 H. Yang, Z. Jin, H. Hu, G. Lu and Y. Bi, *Catalysts*, 2017, **7**, 99.
67 Q. Zhang, X. Quan, H. Wang, S. Chen, Y. Su and Z. Li, *Sci. Rep.*, 2017, **7**, 3128.
68 Q. Zhang, H. Wang, S. Chen, Y. Su and X. Quan, *RSC Adv.*, 2017, **7**, 13223–13227.
69 C. Liu, J. Wang, S. Yang, X. Li and X. Lin, *RSC Adv.*, 2019, **9**, 8065–8072.
70 Q. Cheng, Y. He, Y. Ge, J. Zhou and G. Song, *Microchim. Acta*, 2018, **185**, 332.
71 X. Fan, Y. Su, D. Deng and Y. Lv, *RSC Adv.*, 2016, **6**, 76890–76896.
72 X. Fan, Y. Feng, Y. Su, L. Zhang and Y. Lv, *RSC Adv.*, 2015, **5**, 55158–55164.
73 J. Zhou, Y. Yang and C. Y. Zhang, *Chem. Commun.*, 2013, **49**, 8605–8607.
74 M. H. Chan, C. W. Chen, I. J. Lee, Y. C. Chan, D. Tu, M. Hsiao, C. H. Chen, X. Chen and R. S. Liu, *Inorg. Chem.*, 2016, **55**, 10267–10277.
75 G. Bai, Z. Song, H. Geng, D. Gao, K. Liu, S. Wu, W. Rao, L. Guo and J. Wang, *Adv. Mater.*, 2017, **29**, 1606843.
76 J. Su, L. Zhu, P. Geng and G. Chen, *J. Hazard. Mater.*, 2016, **316**, 159–168.
77 P. Fageria, S. Uppala, R. Nazir, S. Gangopadhyay, C. H. Chang, M. Basu and S. Pande, *Langmuir*, 2016, **32**, 10054–10064.
78 J. Su, L. Zhu and G. Chen, *Appl. Catal., B*, 2016, **186**, 127–135.
79 J. Yu, J. Lei, L. Wang, C. Guillard, J. Zhang, Y. Liu and M. Anpo, *Res. Chem. Intermed.*, 2019, **45**, 4237–4247.
80 S. Liu, L. Wang, J. Tian, J. Zhai, Y. Luo, W. Lu and X. Sun, *RSC Adv.*, 2011, **1**, 951.
81 Y. Tang, Y. Su, N. Yang, L. Zhang and Y. Lv, *Anal. Chem.*, 2014, **86**, 4528–4535.
82 S. Barman and M. Sadhukhan, *J. Mater. Chem.*, 2012, **22**, 21832.
83 X. Cao, J. Ma, Y. Lin, B. Yao, F. Li, W. Weng and X. Lin, *Spectrochim. Acta, Part A*, 2015, **151**, 875–880.
84 S. Liu, J. Tian, L. Wang, Y. Luo and X. Sun, *RSC Adv.*, 2012, **2**, 411–413.
85 D. Xiao, D. Yuan, H. He and J. Lu, *Luminescence*, 2013, **28**, 612–615.
86 H. Abdolmohammad-Zadeh and E. Rahimpour, *Sens. Actuators, B*, 2016, **225**, 258–266.
87 D. Xiao, S. Li, S. Liu, H. He and J. Lu, *New J. Chem.*, 2016, **40**, 320–324.
88 S. Liu, J. Tian, L. Wang, Y. Luo, J. Zhai and X. Sun, *J. Mater. Chem.*, 2011, **21**, 11726–11729.
89 Q. Cheng, X. Liu, Y. He, Y. Ge, J. Zhou and G. Song, *J. Fluoresc.*, 2019, **29**, 719–726.
90 T. An, J. Tang, Y. Zhang, Y. Quan, X. Gong, A. M. Al-Enizi, A. A. Elzatahry, L. Zhang and G. Zheng, *ACS Appl. Mater. Interfaces*, 2016, **8**, 12772–12779.
91 Q. Wang, X. Liu, L. Zhang and Y. Lv, *Analyst*, 2012, **137**, 5392.
92 X. Zhai, P. Zhang, C. Liu, T. Bai, W. Li, L. Dai and W. Liu, *Chem. Commun.*, 2012, **48**, 7955–7957.
93 H. Zhu, X. Wang, Y. Li, Z. Wang, F. Yang and X. Yang, *Chem. Commun.*, 2009, 5118–5120.
94 B. C. Martindale, G. A. Hutton, C. A. Caputo and E. Reisner, *J. Am. Chem. Soc.*, 2015, **137**, 6018–6025.
95 H. He, J. Li, Y. Liu, Q. Liu, F. Zhan, Y. Li, W. Li and J. Wen, *Nano*, 2017, **12**, 1750064.
96 Y. Zheng, L. Lin, B. Wang and X. Wang, *Angew. Chem., Int. Ed.*, 2015, **54**, 12868–12884.
97 P. E. Keivanidis, S. Baluschev, T. Miteva, G. Nelles, U. Scherf, A. Yasuda and G. Wegner, *Adv. Mater.*, 2003, **15**, 2095–2098.
98 J. Shen, Y. Zhu, C. Chen, X. Yang and C. Li, *Chem. Commun.*, 2011, **47**, 2580–2582.
99 Y. Su and Y. Lv, *RSC Adv.*, 2014, **4**, 29324.
100 Y. Su, Y. Xie, X. Hou and Y. Lv, *Appl. Spectrosc. Rev.*, 2013, **49**, 201–232.
101 X. Wang, N. Na, S. Zhang, Y. Wu and X. Zhang, *J. Am. Chem. Soc.*, 2007, **129**, 6062–6063.
102 Z. Li, B. Li, S. Peng, D. Li, S. Yang and Y. Fang, *RSC Adv.*, 2014, **4**, 35144–35148.
103 M. Zhang, Y. Zhang, L. Tang, G. Zeng, J. Wang, Y. Zhu, C. Feng, Y. Deng and W. He, *J. Colloid Interface Sci.*, 2019, **539**, 654–664.
104 D. Qu, J. Liu, X. Miao, M. Han, H. Zhang, Z. Cui, S. Sun, Z. Kang, H. Fan and Z. Sun, *Appl. Catal., B*, 2018, **227**, 418–424.
105 S. Sun and W. Wang, *RSC Adv.*, 2014, **4**, 47136–47152.
106 W. Fang and W. Shangguan, *Int. J. Hydrogen Energy*, 2019, **44**, 895–912.
107 T. Wang, X. Liu, Q. Men, W. Ma, Z. Liu, Y. Liu, C. Ma, P. Huo and Y. Yan, *Spectrochim. Acta, Part A*, 2019, **213**, 19–27.
108 X. B. Cao, L. Gu, L. J. Zhuge, W. J. Gao, W. C. Wang and S. F. Wu, *Adv. Funct. Mater.*, 2006, **16**, 896–902.

